



HAL
open science

Simulation of Optical Properties and Direct and Indirect Radiative Effects of Smoke Aerosols Over Marine Stratocumulus Clouds During Summer 2008 in California With the Regional Climate Model RegCM

Marc Mallet, Fabien Solmon, Laurent Roblou, F. Peers, Solène Turquety, Arnaud Waquet, H. Jethva, O. Torres

► To cite this version:

Marc Mallet, Fabien Solmon, Laurent Roblou, F. Peers, Solène Turquety, et al.. Simulation of Optical Properties and Direct and Indirect Radiative Effects of Smoke Aerosols Over Marine Stratocumulus Clouds During Summer 2008 in California With the Regional Climate Model RegCM. *Journal of Geophysical Research: Atmospheres*, 2017, 122, pp.10,312-10,337. 10.1002/2017JD026905 . insu-03668334

HAL Id: insu-03668334

<https://insu.hal.science/insu-03668334>

Submitted on 16 May 2022

HAL is a multi-disciplinary open access archive for the deposit and dissemination of scientific research documents, whether they are published or not. The documents may come from teaching and research institutions in France or abroad, or from public or private research centers.

L'archive ouverte pluridisciplinaire **HAL**, est destinée au dépôt et à la diffusion de documents scientifiques de niveau recherche, publiés ou non, émanant des établissements d'enseignement et de recherche français ou étrangers, des laboratoires publics ou privés.

Copyright

RESEARCH ARTICLE

10.1002/2017JD026905

Key Points:

- This work provides original analyses on the radiative impact of smoke over stratocumulus coastal region, which is known to be poorly represented by GCM
- This work investigates also the interaction between biomass-burning particles and clouds over coastal stratocumulus region
- This work underlines the great potential of new original satellite products over cloudy regions in addition to regional model outputs

Supporting Information:

- Supporting Information S1

Correspondence to:

M. Mallet,
marc.mallet@meteo.fr

Citation:

Mallet, M., Solmon, F., Roblou, L., Peers, F., Turquety, S., Waquet, F., ... Torres, O. (2017). Simulation of optical properties and direct and indirect radiative effects of smoke aerosols over marine stratocumulus clouds during summer 2008 in California with the regional climate model RegCM. *Journal of Geophysical Research: Atmospheres*, 122, 10,312–10,337. <https://doi.org/10.1002/2017JD026905>





Received 6 APR 2017

Accepted 7 SEP 2017

Accepted article online 15 SEP 2017

Published online 5 OCT 2017

Simulation of Optical Properties and Direct and Indirect Radiative Effects of Smoke Aerosols Over Marine Stratocumulus Clouds During Summer 2008 in California With the Regional Climate Model RegCM

M. Mallet¹ , F. Solmon^{2,3}, L. Roblou³, F. Peers⁴, S. Turquety⁵ , F. Waquet⁶ , H. Jethva^{7,8}, and O. Torres⁸ 

¹CNRM, Météo-France CNRS, UMR 3580, Toulouse, France, ²The Abdus Salam International Center for Theoretical Physics, Trieste, Italy, ³Laboratoire d'Aérodologie, Université de Toulouse, CNRS, UPS, Toulouse, France, ⁴College of Engineering, Mathematics and Physical Sciences, University of Exeter, Exeter, UK, ⁵Laboratoire d'Optique Atmosphérique, CNRS, UMR 8518, Université de Lille, Lille, France, ⁶Laboratoire Optique Atmosphérique, UMR, Lille, France, ⁷Universities Space Research Association, Columbia, MD, USA, ⁸NASA Goddard Space Flight Center, Greenbelt, MD, USA

Abstract The regional climate model RegCM has been modified to better account for the climatic effects of biomass-burning particles. Smoke aerosols are represented by new tracers with consistent radiative and hygroscopic properties to simulate the direct radiative forcing (DRF), and a new parameterization has been integrated for relating the droplet number concentration to the aerosol concentration for marine stratocumulus clouds (Sc). RegCM has been tested during the summer of 2008 over California, when extreme concentration of smoke, together with the presence of Sc, is observed. This work indicates that significant aerosol optical depth (AOD) (~1–2 at 550 nm) is related to the intense 2008 fires. Compared to Ozone Monitoring Instrument (OMI) and Moderate Resolution Imaging Spectroradiometer, the regional pattern of RegCM AOD is well represented although the magnitude is lower than satellite observations. Comparisons with Polarization and Directionality of Earth Reflectances (POLDER) above-clouds aerosol optical depth (ACAOD) show the ability of RegCM to simulate realistic ACAOD during the transport of smoke above the Pacific Ocean. The simulated single scattering albedo is ~0.90 (at 550 nm) near biomass-burning sources, consistent with OMI and POLDER, and smoke leads to shortwave heating rates ~1.5–2°K d⁻¹. RegCM is not able to correctly resolve the daily patterns in cloud properties notably due to its coarse horizontal resolutions. However, the changes in the sign of the DRF at top of atmosphere (TOA) (negative to positive) from clear-sky to all-sky conditions is well simulated. Finally, the “aerosol-cloud” parameterization allows simulating an increase of the cloud optical depth for significant concentrations, leading to large perturbations of radiative fluxes at TOA.

1. Introduction

Atmospheric aerosols are known to influence the radiative balance at regional and global scales through their interactions with clouds (first and second aerosol indirect effect, AIE) and solar to infrared radiations (direct radiative forcing, DRF). The feedbacks of the absorption of solar radiations due to absorbing particles (smoke, pollution and mineral dust) on cloud microphysical properties (semidirect effect) is also recognized as an important radiative perturbation (Ackerman et al., 2000; Johnson et al., 2004). Although AIE represents the main uncertainty among the different radiative forcings (Forster et al., 2007; IPCC, 2013), the simulation of direct and semidirect effects attributable to absorbing particles still remain challenging for regional (RCM) and global climate models (GCM). For example, large uncertainties persist in the estimation of aerosol absorbing optical depth (AAOD) by GCMs over regions characterized by important concentration of absorbing particles such as South America, Southern Africa, and East Asia (Shindell et al., 2013). Over these regions, large negative biases are observed in simulated AAOD leading to significant uncertainties on the estimation of aerosol direct and semidirect effects. Recent studies based on remote sensing have shown that the large positive shortwave (SW) DRF at top of atmosphere (TOA) attributable to smoke over the southeastern Atlantic Ocean (which can peak at +130 W m⁻², DeGraaf et al., 2012) is not well reproduced by GCMs (DeGraaf et al., 2014). A large intermodel spread in the TOA DRF has been pointed out over this region for

GCMs and chemical transport models involved in the AeroCOM (Aerosol Comparisons between Observations and Models) project (Myhre et al., 2013; Stier et al., 2013). Such studies reveal the difficulty of correctly representing the direct effect of absorbing aerosols, especially when transported above highly reflective marine stratocumulus clouds (Sc).

In that context, the Californian, Chilean, and Namibian coastal regions of the Pacific and Atlantic Oceans are of great interest since they are characterized by both the presence of anthropogenic (pollution and smoke) absorbing particles and persistent Sc (Wood, 2012), which are known to be essential in the global radiative budget. Sc approximately cover one fifth of Earth's surface in the annual mean (23% of the ocean surface and 12% of the land surface) and tend to be located along the eastern peripheries of the major oceans (Wood, 2012). Sc are characterized by large albedo and strongly reflect incoming solar radiation (Chen et al., 2000), while they exert only a small effect on outgoing longwave radiation. Hence, they exert a strong negative net radiative effect and only small changes in their macrophysical (coverage and thickness) or microphysical (cloud effective radius (CER), cloud optical depth (COD), or liquid water path (LWP)) properties are required to produce a radiative effect comparable to those associated with increasing greenhouse gases (Randall et al., 1984). This comes in addition to the complex and uncertain DRF and semidirect effects associated with absorbing aerosol discussed above.

Modeling studies over such specific regions are thus especially relevant, from highly resolved large eddy simulations (Johnson et al., 2004) to GCM ($x \sim 100\text{--}200$ km). RCM are particularly interesting as they allow addressing seasonal to decadal time scales with an improved representation of regional features such as aerosol sources and plume gradients, coastal transition and dynamics, or mesoscale weather patterns. In complement to GCM approaches, RCM can also allow the study of regional feedbacks to radiative perturbations, with the caveat of not accounting for large-scale dynamical adjustments (Rodwell & Jung, 2008) due to imposed boundary conditions.

In that general context, our study focuses more specifically on the Californian coastal region, which is among the U.S. states showing the highest wildfire activity, generally starting mid-May and ending in October (Pfister et al., 2008). In addition, the wildfire activity in the western U.S. has increased in recent decades mainly due to combination of severe droughts (Westerling et al., 2006). The transport pattern of biomass burning in coastal California leads to regular mixing of smoke within Sc (Brioude et al., 2009), which are common during summer in the eastern North Pacific Ocean (with a maximum in June, Klein & Hartmann, 1993). These particular situations are favorable to aerosol-cloud interactions and indirect effects, but fewer studies have addressed the estimation of the different radiative effects of smoke over California using a RCM approach.

The main objective of this work is to study the optical properties of smoke and the associated direct and indirect radiative effects over California using the RegCM model (Giorgi et al., 2012). In section 2, we propose an improvement of the representation of smoke particles, their radiative properties, and their interactions with Sc. Section 3 describes numerical model experiment and evaluation data sets. In section 4, the model is tested and evaluated for summer 2008, for which 2,780 individual fires had been observed over Northern California, burning a surface of 4,686 km² (Gyawali et al., 2009). The SW aerosol optical depth, absorbing properties (AAOD and single scattering albedo (SSA)), heating rate, cloud microphysical (i.e., cloud optical depth; COD, cloud droplet number concentration (CDNC), and CER) properties, and the SW DRF (in clear-sky and all-sky conditions) exerted at TOA are analyzed and discussed. The main conclusions are summarized in section 5.

2. New Developments in RegCM

2.1. Aerosol Scheme

The basic aerosol scheme accounts for sulfate, organic and black carbon, and dust and sea-salt particles and is described by Giorgi et al. (2012) and Solmon et al. (2006, 2008). The model assumes an external mixture of particles and includes advection by atmospheric winds, diffusion by turbulence, vertical transport by deep convection, surface emissions, dry and wet (in-cloud and below cloud) removal processes, and gas and aqueous phase chemical conversion mechanisms. In this model, dust and sea-salt emissions are based on Zakey et al. (2006a, 2006b) with the latest modifications described in Giorgi et al. (2012) and Solmon et al. (2015). Different studies have shown the ability of RegCM to reproduce the basic regional patterns and

seasonality of aerosols over Europe (Zanis et al., 2012), Western Africa (Malavelle et al., 2011; Solmon et al., 2008, 2012; Tummon et al., 2010), or India (Solmon et al., 2015). Recently, the thermodynamic equilibrium model ISORROPIA has been coupled with RegCM to estimate the inorganic aerosol concentrations (Li et al., 2016), while a treatment of secondary organic aerosols (SOA) has been proposed by Yin et al. (2015). Concerning primary black and organic carbon species, a bulk approach is applied where aerosol size distribution is assumed for calculating aerosol properties (Solmon et al., 2006), while for primary mineral dust and sea salt, a more explicit size representation is used based on 4 or 12 (dust) bins (Tsikerdekis et al., 2017) and 2 (sea-salt) bins. As mentioned previously, particles are treated as externally mixed. This represents a limitation with regard to black carbon (BC) mixing (internal/external) state, which can significantly affect absorption (Jacobson, 2000). Knowing that, specific attention is being paid in this study to the characterization of absorbing properties (AAOD and SSA) of smoke simulated by RegCM as well as the associated SW heating rate.

The radiative properties (mass extinction efficiency (MEE), SSA, and asymmetry parameter) of each aerosol species are calculated for the different spectral bands of the rapid radiative transfer model (RRTM) SW and longwave scheme (Mlawer et al., 1997). Aerosol DRF at the surface and at TOA, for both clear-sky (aerosol forcing with a cloudless column) and all-sky (clouds and aerosol) conditions, is diagnosed using a double call (with and without aerosols) to the RRTM during the RegCM model integration. The semidirect radiative effect, which represents the modifications of the cloud properties due to absorbing aerosols, is not analyzed in the present study. In its current version, smoke aerosols are represented by two different tracers (primary BC and organic carbon (OC)) with fixed microphysical and radiative properties without any consideration of possible differences between fossil fuel versus biomass-burning emissions. This hypothesis implies that aerosol radiative properties are similar for both anthropogenic and smoke BC/OC emissions.

Concerning the “aerosol-cloud” interactions, an approach based on simple parametrizations is used in a similar way as in most GCMs. This allows keeping numerical costs low, necessary for climate and ensemble simulations. The activation of hydrophilic particles to cloud droplets is not resolved. In RegCM, the first indirect effect is presently implemented for anthropogenic sulfates only (Qian & Giorgi, 1999) and the impact of aerosols on liquid clouds via the second indirect effect (precipitation modulation due to hygroscopic aerosols) is currently under development but not activated here. Recent developments have been also proposed for the treatments of the first and second radiative effects (Li et al., 2016).

Classically, the first indirect effect is represented in RegCM using a simple relationship relating the mass (or number) of hydrophilic aerosols to the cloud droplet number concentration (CDNC). In the presence of sulfate aerosols, the method of Hegg (1994) is applied to estimate CDNC as a function of calculated sulfate mass mixing ratio (Qian & Giorgi, 1999). In a second step, CDNC is used to calculate the cloud droplet effective radius (CER) through the following relation:

$$CER = (3L/4\pi\rho_w kCDNC)^{1/3} \tag{1}$$

where L is the cloud water content, ρ_w is the density of water, and k is the cube of the ratio of the mean volume radius and the effective radius of the cloud droplet spectrum, which is assumed to be equal to 0.67 over continent and 0.80 over ocean (Martin et al., 1994). In the current version and in the absence of anthropogenic sulfate particles, CER is fixed to the value of 10 μm over oceans, typical of clouds determined by a background cloud condensation nuclei (CCN) population (Briegleb, 1992), while over land it is given as a function of temperature (Alexandri et al., 2015). The radiative properties of liquid clouds, in the shortwave spectral region, are given by the following parameterizations (Briegleb, 1992):

$$COD(\lambda) = CWP[a(\lambda) + (b(\lambda)/CER)] \tag{2}$$

$$SSA(\lambda) = 1 - c(\lambda) - d(\lambda) \times CER \tag{3}$$

$$g(\lambda) = e(\lambda) + f(\lambda) CER \tag{4}$$

where λ denotes the spectral interval and CWP the cloud water path. Hence, two parallel simulations, modifying or not the CER, allow the determination of cloud albedo.

2.2. Inclusion of New Smoke Radiative Properties for DRF Calculations

Two new tracers are implemented in RegCM, describing respectively the mass concentration of fresh and aged smoke aerosols. Aging from the fresh mode to hygroscopic aged is quantified using an e -folding

Table 1

Parameters Describing Aerosol Components in the RegCM Models for the Two Smoke Tracers and the Resulting Aerosol Optical Properties, Based on Bellouin et al. (2011)

Aerosol components	r_0	σ	Density	m	MEE	SSA
Fresh smoke	0.10	1.30	1,350	1.55–0.029i	4.2/4.8/8.4	0.84/0.85/0.92
Aged smoke	0.12	1.30	1,350	1.54–0.018i	5.1/6.5/16.	0.91/0.92/0.97

Note. Here r_0 and σ are the median radius (in μm) and geometric standard deviation of the lognormal distribution. Mass density is reported in kg m^{-3} , m is the complex refractive index, and MEE and SSA the mass extinction efficiency and single scattering albedo in dry state and reported at 550 nm. The values for MEE and SSA are reported here at 0%, 60%, and 100% of relative humidity.

time of 6 h according to Abel et al. (2003). For each tracer, dry-state aerosol size distributions are assumed based on lognormal function (Table 1) similar to those implemented in the Hadley Centre global climate model, HadGEM2-ES (Bellouin et al., 2011). The refractive indices (in dry state) of smoke are also indicated in Table 1. Radiative properties at different wavelengths in the solar spectral range are calculated for the specific wavelength bands of the RRTM. The calculated radiative properties are the following: the mass extinction and absorption efficiencies (MEE and MAE, in $\text{m}^2 \text{g}^{-1}$), single scattering albedo (SSA), and asymmetry parameter (g). The values in the visible (VIS) and near infrared spectral ranges are reported in the supporting information (Figure S1). At 550 nm and in dry state, the calculated radiative properties are 5.0 (6.0) $\text{m}^2 \text{g}^{-1}$, 0.81 (0.90), and 0.67 (0.80) for MEE, SSA, and g , for fresh (aged) smoke tracers, respectively (Table 1).

Smoke particles are known to be hydrophilic (Rissler et al., 2006), and the dependence of the radiative properties to relative humidity (RH) has been included for both tracers. This dependence is formulated as for sulfate aerosols (Solmon et al., 2006).

$$\text{MEE}_{\text{wet}} = \text{MEE}_{\text{dry}}(1 - \text{RH})^{-\alpha} \quad (5)$$

where MEE_{wet} and MEE_{dry} are for wet and dry conditions. We have selected a value of 0.26 and 0.15 for the parameter α in order to reproduce the changes of MEE with RH for aged and fresh smoke, respectively (not shown, Figure S1 in the supporting information). At very high humidity ($\text{RH} > 99\%$) maximum thresholds of 8.5 and 16.9 $\text{m}^2 \text{g}^{-1}$ are considered for fresh and aged smoke, in order to avoid unrealistic values of MEE. In a similar way, we have also implemented a dependence of smoke SSA on RH.

$$\text{SSA}_{\text{wet}} = \text{SSA}_{\text{dry}}(1 - \text{RH})^{-\alpha} \quad (6)$$

where SSA_{wet} and SSA_{dry} are for wet and dry conditions. Here the values of α have been fixed to 0.015 (0.02) for aged (fresh) smoke to represent the variations of smoke SSA with RH (Figure S1 in the supporting information) as reported in Bellouin et al. (2011). Contrary to MEE and SSA, there is no correction of the asymmetry parameter (ASP) with RH in our simulations due to the absence, to our knowledge, of available data for smoke particles. Our simulations indicate that the ASP values (at 550 nm) simulated near sources are about ~ 0.55 and ~ 0.58 – 0.60 during the transport, which are close to climatological Aerosol Robotic Network (AERONET) observations (~ 0.60 at 550 nm) for biomass-burning particles (Dubovik et al., 2002). However, due to its importance on the estimation of the direct radiative forcing and as ASP is sensitive to RH (Zhuang et al., 2017), sensitivity tests have been performed by perturbing ASP by $\pm 10\%$ to quantify the uncertainties related to this hypothesis. The results (not shown, Figure S2 in the supporting information) indicate that the SW TOA DRF can be increased by about $+5 \text{ W m}^{-2}$ (ASP increased by 10%).

2.3. Implementation of the First Indirect Effect of Smoke for Stratocumulus Clouds

The prediction of CDNC in regional and global model remains a challenging task but is crucial to reduce the uncertainties related to the aerosol first indirect effect. The number of cloud droplets formed in a rising air parcel is dependent on different variables such as the number, size, and chemical composition of aerosols as well as the meteorological conditions (i.e., the updraft velocity). All these factors are highly variable at global scale between different regions and for different cloud regimes within the same region (Pringle et al., 2009). Because of the number of variables carried in climate models, and as microphysical processes in clouds operate on much smaller scales than global or regional model grid cells, the estimation of CDNC is often simplified in such models and involves parameterizations. A widely used approach to represent aerosol-cloud interactions is to define empirical relationships between number (or mass) of

aerosols and CDNC based directly on observations, as proposed by Menon et al. (2008). Such an approach offers a simple and effective way, associated with a reasonable numerical cost to predict CDNC but is associated to important limitations (Pringle et al., 2009). The first is that these relationships do not account for the dependence of the droplet nucleation on aerosol size distribution, chemical composition, and updraft velocity and hence are limited in their applicability. The second is obviously linked to the in situ observations themselves, generally obtained for a limited geographical region, limiting their extrapolation to other regions. Incidentally, such methods, that is, based on in situ observations derived over a particular region, are certainly more adapted to RCM than GCM.

In RegCM and as mentioned in section 1, only sulfate aerosols are able to modify cloud microphysical properties through the first indirect effect even if very recent developments have been also proposed for the treatments of the first and second radiative effects (Li et al., 2016). In this study, we have implemented a linear relationship between CDNC and the accumulation mode number concentration (AMNC) as proposed by Hegg et al. (2012) for marine Sc. The linear relationship is primarily based on aircraft measurements of cloud condensation nuclei (CCN), accumulation and Aitken mode aerosol number concentrations and CDNC obtained for the three large, semipermanent marine Sc decks of the Earth (in the Pacific offshore of California and Chile and in the Atlantic offshore of Namibia). The data used by Hegg et al. (2012) are derived primarily from the multiyear CARMA-II and CARMA-III experiments, conducted off the California coast of North America from 2004 to 2007 (Hegg et al., 2007) and the VOCALS-Rex study conducted off the Chilean coast of South America in 2008 (Allen et al., 2011). Additionally, a small amount of data from the Sc deck off the Namibian coast of Africa has been used from a data archive of the SAFARI 2000 (Haywood et al., 2003) program. Based on these observations, the Hegg et al. (2012) proposed relationship is the following:

$$\text{CDNC} = 0.72 \text{ AMNC} + 47 \quad (7)$$

where AMNC is the number concentration (in cm^{-3}) of aerosols in the accumulation mode.

This relationship indicates that CDNC were typically about ~75% of AMNC in Sc environments, which is consistent with the results obtained by Twohy et al. (2005) during the Dynamics and Chemistry Marine Stratocumulus-II (DYCOMS-II) experiment over the eastern Pacific Ocean, off the coast of San Diego, California. The prognostic tracer mixing ratios X (kg kg^{-1}) are first used to calculate the aerosol mass concentration (AMC, in $\mu\text{g m}^{-3}$) for fresh and aged smoke, using the following relation:

$$\text{AMC} = \rho * X * 10^{-9} \quad (8)$$

where ρ is the density of dry air. In a second step, the aerosol number concentrations (in cm^{-3}) of the two smoke tracers are calculated as

$$\text{AMNC} = \left(106/\rho_p\right)^* (6/\pi)^* (1/D_g^3)^* \text{AMC} * \exp\left(-4.5(\log\sigma)^2\right) \quad (9)$$

where ρ_p is the particle density, D_g the geometric mean diameter, and σ the geometric standard deviation, which are reported in Table 1. The total AMNC is then calculated by adding smoke particles number to sulfate and fine sea salt. The new CDNC is then estimated from equation (4), impacting CER and COD through equation (1), which are used as input to the radiative transfer scheme. As the relationship between CER and CDNC is not a linear function (Twohy et al., 2005) and to avoid unrealistic low CER values possibly calculated under extreme smoke concentrations, a minimum CER is fixed to $3.5 \mu\text{m}$ in RegCM. This value corresponds to the lowest CER reported in Table 2 for in situ observations over California. Finally, in order to quantify uncertainties related to the choice of hygroscopic properties of smoke on microphysical properties of Sc, two additional sensitivity tests have been realized by using hygroscopic efficiencies of 50 and 60%. The results, in terms of CER and CDNC, are discussed in sections 4.4.1 and 4.4.2.

3. Model Configuration and Data Used

3.1. Simulation Designs and Important Physics Options

Simulations extend from 15 June to 15 July, considering a period of 5 days of spin-up as the intense smoke activities starts around 20 June. The simulation uses lateral boundary conditions from National Centers for Environmental Prediction reanalyses (Kalnay et al., 1996). Sea surface temperatures (SST) are

Table 2

Aerosol Number Concentration, Cloud Droplet Number Concentration, Cloud Optical Depth, and Cloud Effective Radius Obtained During the Different Experimental Campaigns for Marine Sc and Over the Californian Region

Aerosol influence	Aerosol concentration (cm ⁻³)	CDNC (cm ⁻³)	COD	CER (μm)	Campaigns/regions	References
Not specified—all	#	40–400	2.5–33	3.8–7.4	CARMA-II and CARMA-III/Californian coast	Hegg et al. (2007)
Ship emissions	#	100–140	43.6–67.3 ^a	6.9–9.7	FIRE IFO/coast of Southern California	King et al. (1993)
Not specified—all	160–530	50–300	7–40	4.5–12	DYCOMS-II/off the coast of San Diego, California	Twohy et al. (2005)
Not specified	#	200–800	20–40	4–8	MASRAD/Point Reyes, California	McComiskey et al. (2009)

^aEstimated at 0.744 μm.

prescribed as boundary conditions using NOAA OI-SST products (Reynolds et al., 2002). For this simulation, long-range transport of aerosols is not forced at the lateral boundary conditions, and we defined a domain large enough to take into account the main biomass-burning sources during this specific episode. The latter extends from 20 to 55°N and from -135 to -110°W, with a horizontal resolution of 10 km (300 × 250 points in the grid model) and 23 vertical levels (from 1,015 to 10 hPa). A 120 km buffer zone is considered where a relaxation method allows a smooth transition in order to avoid an abrupt change between simulated fields and lateral boundary conditions. The important physical options used for this study are the biosphere-atmosphere transfer (BATS) scheme (Dickinson et al. 1993) and the Grell convection scheme. Of primary importance, we use the University of Washington turbulence scheme, which has been evaluated over the Californian region by O'Brien et al. (2012), showing notably an improvement of the representation of low Sc.

The RRTM radiative transfer scheme is used to calculate interactions between aerosol radiative properties and shortwave and longwave (for coarse dust and sea-salt particles only) radiations. Finally, it should be mentioned that the possible impact of aerosol sea surface dimming on the sea surface temperature (SST), as described in Solmon et al. (2012, 2015), has not been activated here and is outside the scope of this work. This limitation might, however, be of secondary importance here, given the relatively short integration and fact that SST is strongly driven by ocean dynamics in upwelling region.

For atmospheric particles sources, the daily biomass-burning emissions from the APIFLAME emissions model are used (Turquety et al., 2014). For this study, the emissions are calculated based on Moderate Resolution

Imaging Spectroradiometer (MODIS) fire observations at 500 m, combined to MODIS land use classification for the same year, both at 500 m resolution. The biomass burned is derived using biomass density simulated by the ORCHIDEE (Organising Carbon and Hydrology In Dynamic Ecosystems) (Krinner et al., 2005) vegetation and carbon cycle model, and specific emissions are then calculated using factors compiled by Akagi et al. (2011). Here only the emissions of black carbon (BC), organic carbon (OC), and sulfur gaseous SO₂ are used. Smoke particles are emitted at the first vertical level of the model, without any considerations of pyroconvective processes, as no clear consensus of such processes exist over the region of interest. For example, Labonne et al. (2007) have showed that smoke plumes are generally confined in the planetary boundary layer near smoke sources. Accordingly, smoke emissions have been used to force the model at the first model level following the recommendations from the first phase of AeroCom (Dentener et al., 2006, section 7 and Figure 9). Fire emissions from savannah are assumed to have small plume rise and are emitted at the lowest model level, allowing subgrid-scale turbulence to mix these through the boundary layer. One of the limitations concerns the diurnal cycle of smoke emission which is not taken into account, which could impact temporal variations of the aerosol loadings and optical properties (Xu et al., 2016). As mentioned previously, the lateral boundary conditions do not include the possible long-range transport of smoke within the domain used (Figure 1). Although focused on smoke, the RegCM simulations include also different aerosol tracers, which are

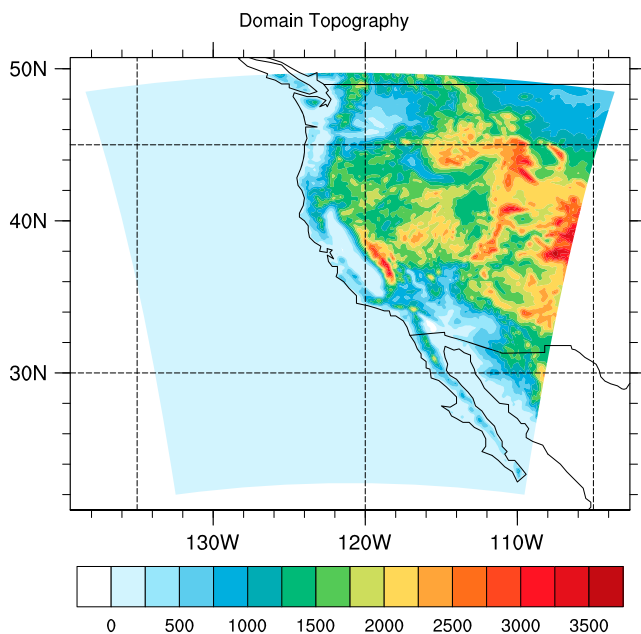


Figure 1. RegCM domain used for the simulation.

Table 3

Satellite and Reanalyses Data Used in This Work to Evaluate the RegCM Simulations of Aerosol and Cloud Properties (the Horizontal and Temporal Resolution Are Reported)

	Aerosol variables	Cloud variables	Spatial resolution	Temporal resolution
MYD08_D3	AOD	CER, COD	1°	Daily
MATDMOS	AOD	CER, CF	10 km	Daily
OMI	AOD, AAOD, ACAOD	#	1°	Daily
POLDER	ACAOD, ACSSA, ACDRF	#	18.5 km	Daily
MERRA reanalyses	#	CF	0.5° × 0.625°	3 h
MACC reanalyses	AOD, AAOD, DRF	AIE	1.125°	Daily

Note. The above-cloud DRF (ACDRF), DRF, and aerosol indirect effect (AIE) are reported at TOA and in the SW spectral ranges.

secondary sulfate (SO₄) produced from SO₂ oxidation and mineral dust (represented by four different bins here, with two in the accumulation and two in the coarse size fraction).

Through aging, biomass-burning particles mass is known to increase due to the condensation of volatile organic compounds. However, and in the absence of secondary organic aerosols (SOA) production in RegCM, a correction factor (i.e., ratio of organic matter (OM) to primary OC) has been used for artificially representing SOA formation within the smoke plume. The lack of a complete representation of SOA in current climate models obviously represents an important source of uncertainties in the estimation of the smoke aerosol concentration (Johnson et al., 2016). At this time, referenced values of this ratio are scarce and mainly based on Aerosol Mass Spectrometer in situ observations. The average OM to OC ratio is found to be ~2.5 by Bougiatioti et al. (2014) over a remote Mediterranean background site, which is consistent with the value (2.2) reported by Hildebrandt et al. (2010). In addition, Sciare et al. (2005) indicate a value of 2.1 to convert OC to OM for a mass reconstruction during summer over the Eastern Mediterranean. For example, the value of 1.6 is actually retained in the HadGem global model (Bellouin et al., 2011, Johnson et al., 2016). In this work, the OM to OC ratio of 2.0 has been used and represents an average of published values. This correction factor has been applied directly to the emissions of primary OC. In order to quantify the uncertainties related to the OC to particulate organic matter (POM) ratio, some sensitivity tests have been performed using two different values (1.5 and 2.5) and show an impact of ±0.2 (not shown, Figure S3 in the supporting information) in calculated aerosol optical depth (AOD) (at 550 nm). Finally, it should be recalled that the possible influence of brown carbon particles, especially for ultraviolet (UV) radiations, has not been taken into account in the present simulation. Such aspect is outside of the topic of this study, but further developments are scheduled in a future version of RegCM.

Different aerosol and cloud properties, estimated from surface and (passive and active) satellite remote sensing techniques, as well as reanalysis data, have been used in this work for evaluating RegCM simulations. They are presented in the following parts and summarized in Table 3.

3.2. Monitoring Atmospheric Composition and Climate and Modern-Era Retrospective Analysis for Research and Applications-II Aerosol and Clouds Reanalysis

The European Center for Medium-Range Weather Forecasts (ECMWF) has developed a reanalysis of global atmospheric composition since 2003, which includes the five main aerosol species. The first generation of ECMWF reanalysis (Morcrette et al., 2009), issued by the GEMS (Global and regional Earth-System (atmosphere) Monitoring using Satellite and in situ data) project, covers the period 2003–2008. The Monitoring Atmospheric Composition and Climate (MACC) is the second-generation product and provides improvements in sulfate distributions and has extended to the 2003–2011 period (Benedetti et al., 2009). Here we use MACC daily data sets at 1.125° resolution, including anthropogenic aerosol, mineral dust, and sea-salt AOD (at 550 nm); anthropogenic and mineral dust AAOD (at 550 nm); and anthropogenic SW direct and indirect forcing (at TOA) in all-sky conditions (Table 3). In MACC, the indirect forcing calculation is based on the change in cloud albedo exerted by a change in cloud droplet number concentration due to anthropogenic aerosols (Quaas et al., 2008). In addition, we have used the Modern-Era Retrospective Analysis for Research and Applications (MERRA) reanalysis, which was generated with version 5.2.0 of the Goddard Earth Observing System (GEOS) atmospheric model and data assimilation system (DAS). The system, the input

data streams and their sources, and the observation and background error statistics are fully documented in Rienecker et al. (2011). In the present work, we have only used the cloud fraction product at 1,000 hPa, at $0.5^\circ \times 0.625^\circ$ spatial resolution (Table 3). It should be recalled that especially due to their coarser horizontal resolutions, reanalyses generally underestimate the cloud fraction and boundary layer depth in the eastern Pacific.

3.3. Ozone Monitoring Instrument, POLDER, and MODIS Products for Aerosols and Clouds

We use the Ozone Monitoring Instrument (OMI) sensor, operating since October 2004 onboard of the EOS Aura satellite, which is a spectrometer with high spectral resolution (Levelt et al., 2006). OMI offers nearly global daily coverage with a spatial resolution for the UV-2 and VIS (UV-1) channels ranging from $13 \times 24 \text{ km}^2$ at nadir. Here we use data from the OMAERUV_v003 product containing retrievals from the OMI near-UV algorithm (Torres et al., 2007). This algorithm derives a variety of aerosol radiative properties, such as an aerosol index (AI), AOD, AAOD (uncertainty of $\pm (0.05 + 30\%)$), and SSA (uncertainty of ± 0.03) for clear-sky conditions. For this study, we used SSA retrieved at 380 and 500 nm (Table 3). OMI above-clouds aerosol optical depth (ACAOD) (Jethva et al., 2016) have been also analyzed.

MODIS level 2 and 3 daytime products at 10 km and 1° resolution, respectively, are used for evaluating aerosol and cloud properties (Table 3). Data sets include AOD, liquid COD, and liquid CER. The accuracies of MODIS aerosol and cloud optical depth measurements are about 0.05 over the ocean and 0.15 over the land, respectively (Remer et al., 2005). The MODIS uncertainty for CER is $\sim 10\%$ but can be larger depending on the corresponding COD, vertical homogeneity, and solar/viewing geometry (Nakajima et al., 2010). Comprehensive MODIS validation has been reported by Painemal and Zuidema (2011) and showed high correlations between MODIS COD, CER, and in situ measurements. Zhang and Platnick (2011) found that CER computed using three different MODIS bands were consistent within $\pm 2 \mu\text{m}$ for spatially homogeneous coastal Sc, which is the cloud regime studied here.

In addition, the POLDER (Polarization and Directionality of Earth Reflectances) retrieval combines the sensitivity of multidirectional polarized and total radiances to the presence of aerosol above liquid clouds. The $6 \times 6 \text{ km}^2$ POLDER products come from the PARASOL (Polarization and Anisotropy of Reflectances for Atmospheric Science coupled with Observations from a Lidar) Collection 2 v03.02. To ensure the quality of the products, several filters are applied to reject, notably, inversions associated with $\text{COD} < 3$ and/or inhomogeneous clouds, as defined by Waquet, Cornet, et al. (2013). A detailed description of the POLDER method and the filters is provided by Waquet, Cornet, et al. (2013), Waquet, Peers, et al. (2013), and Peers et al. (2015). The aerosol and cloud properties (i.e., the COD, the above-cloud AOD, and SSA) retrieved by POLDER are then used to calculate the instantaneous direct radiative effect (DRE) of aerosols above clouds. The procedure is described in Peers et al. (2015).

3.4. Surface AERONET Data

AERONET (Aerosol Robotic Network) is a well-known federated network of ground-based Sun photometers and the associated data inversion and archive system that routinely performs direct Sun observations and both almucantar and principal plane sky radiance measurements, to retrieve and distribute global aerosol columnar properties. Along with AOD observations, the AERONET aerosol retrieval algorithm (Dubovik & King, 2000) delivers the complete set of column-effective aerosol microphysical parameters, including volume size distribution, refractive index at four wavelengths (440, 670, 870, and 1,020 nm), and fraction of spherical particles (Dubovik et al., 2006). In addition, using these microphysical parameters, the retrieval algorithm provides other column-effective aerosol optical properties, such as wavelength-dependent SSA, phase function, and asymmetry parameter (Dubovik et al., 2002). In the present study, we have used the AOD, AAOD, and SSA for AERONET level 2.0 inversion products. The uncertainty of retrieved AAOD is estimated at the level of ± 0.01 at wavelengths 440 nm and greater, whereas SSA uncertainty is estimated to be ± 0.03 for $\text{AOD} > 0.2$ and ± 0.07 for $\text{AOD} < 0.2$ (Dubovik et al., 2000, 2002).

4. Results

4.1. Stratocumulus Cloud Macrophysical-Microphysical Properties

Although this study is not dedicated to the evaluation of simulated Sc (already discussed in O'Brien et al., 2012), we have conducted some comparisons on cloud macrophysical properties (cloud fraction (CF) and

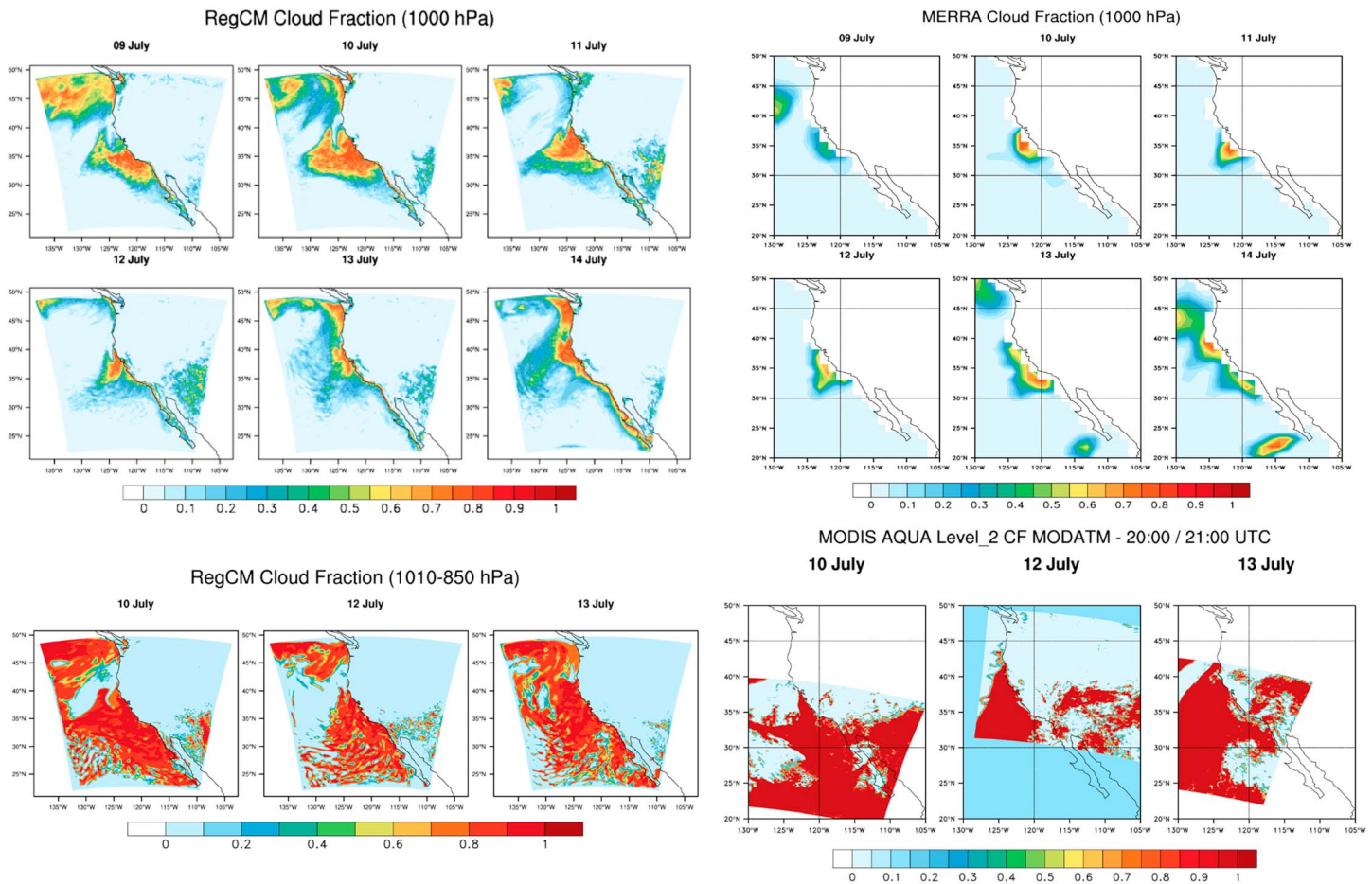


Figure 2. (top left) RegCM model and (top right) MERRA reanalysis of the cloud fraction (CF) estimated at 1,000 hPa and for the 9 to 14 July period. (bottom left) RegCM (calculated using the random overlap assumption over the 1,010–850 hPa vertical levels) and (bottom right) MODIS (Level 2) CF are also reported for 10, 12, and 13 July.

vertical extend). To do so, we have compared CF calculated by RegCM with CF obtained from the MERRA (Naud et al., 2014) reanalyses, both of them at 1,000 hPa. The CF estimated by RegCM and MERRA are reported in Figure 2 (from 9 to 14 July).

The spatial resolution of MERRA reanalyses does not allow to detect CF near the coast, limiting the comparisons over this zone. However, we obtain a reasonable representation of CF by RegCM in terms of spatial patterns and order of magnitude, and in both cases, CF higher than 0.5–0.6 are generally observed off the coast of California. During this period, CF is relatively well simulated, especially for 10 and 12 July, where spatial patterns and amplitudes (CF higher than 0.7) are captured. For 11 July, the regional pattern is, however, not captured by the model, which simulates higher CF for Northern California compared to MERRA reanalyses. For 9, 13, and 14 July, it is somehow difficult to evaluate the ability of RegCM to simulate CF, as most of Sc are observed close to the Californian coast where MERRA information is missing. Away from the coast, Figure 2 shows that CF are reasonably represented by RegCM with values around 0.5–0.7, consistent with MERRA reanalyses. For these days, we can also note higher simulated CF over oceans compared to MERRA reanalyses.

In addition to reanalyses, we have also used Level 2 (resolution of 10 km) MODIS CF products. Figure 2 indicates the CF retrieved by MODIS and calculated by RegCM for 10, 12, and 13 July (the MODIS CF for the whole period is provided in the supporting information, Figure S4). RegCM values are calculated using the random overlap assumption (Oreopoulos & Khairoutdinov, 2003) for the atmospheric levels between 1,010 and 850 hPa. The results indicate that the total CF is relatively well reproduced by RegCM with values ~0.8–1 for those days over a large part of the domain. For 12 July, the CF is overestimated by RegCM in the bay of Los Angeles

and for 13 July, some low values (CF ~ 0.2 – 0.3) detected by MODIS near the coast (south of San Francisco) are also overestimated by RegCM. On the contrary, the CF away from the coast (around 120 – 125°W) is underestimated by RegCM maybe due to the presence of middle clouds. This figure indicates that RegCM is able to reproduce the main CF regional pattern even if some bias are identified due to the fact that such regional models are not able to reproduce correctly Sc cloud properties and dynamics (notably due to their coarse horizontal/vertical resolution).

In addition, we have compared LWP derived from MODIS and estimated by RegCM (for atmospheric levels between 975 and 950 hPa) for the whole period (Figure S4 in the supporting information) and for 10 and 13 July (Figure S5). One of the main information is that the calculated LWP are around 25 – 150 g m^{-2} over the whole domain in agreement with those (~ 30 – 150 g m^{-2}) derived by MODIS. However, biases are identified especially in the bay of Los Angeles, and near the coast for 13 July, where LWP is generally overestimated by the model. Away from the coasts, the LWP is consistently simulated, except for 13 July around $\sim 120^\circ\text{W}$.

In parallel to CF and LWP, we have also evaluated the estimated top of Sc by comparing RegCM simulations with Cloud-Aerosol Lidar with Orthogonal Polarization (CALIOP) observations for transects cutting California. Here we just report comparisons for 9 July. Figure 3 represents the simulated aerosol and cloud typing corresponding to CALIOP transect over the region (Figure 3a). CALIOP observations have been obtained at $\sim 10:00$ UTC. Figure 3b indicates the aerosol number concentration in the accumulation mode and the CF simulated by RegCM for the same CALIOP transect. RegCM simulates a CF of about ~ 0.3 – 0.4 between the sea surface and 500 m of altitude near the coast, from 36.5°N to 34°N . The top of Sc is shown to slightly increase away from the Californian coast, from 32°N to 26°N in latitudes. At these latitudes, the Sc top reaches altitudes of about $\sim 1,000$ m. The comparison of the RegCM simulated vertical extends of Sc with CALIOP observations indicates that RegCM is able to correctly simulate the top of marine Sc observed over this region and during this period. CALIOP data indicate also that marine Sc (light blue color in Figure 3a) are confined below 500 m near the Californian coast, in accordance with simulations. CALIOP retrieved Sc top is also shown to increase for latitudes above 32°N as already mentioned for RegCM. Finally, the vertical distribution of smoke particles is reasonably simulated with aerosols located between the sea surface and 6 km high, in agreement with CALIOP observations (orange points). The presence of aerosol at latitudes ~ 26 – 28°N detected by CALIOP (located between 1 and 3 km) is also consistent in the model. Figure 3 indicates a possible separation between the smoke and cloud layers. However, it does not preclude aerosol-cloud interaction as the lidar signal could be attenuated and only sensitive to the top of the aerosol plume. Hence, smoke is possibly transported both within the marine boundary layer (MBL) and above the MBL, confirming that this event represents a good case study for estimating the DRF at TOA and possible interactions between smoke and Sc.

4.2. Simulation of Smoke Radiative Properties

4.2.1. Aerosol Optical Depth—Comparisons With Satellite Retrievals

Figure 4 displays the AOD simulated by RegCM (at 550 nm) from 9 to 14 July over the whole simulation domain. The reported AOD are taken at $21:00$ UTC, which corresponds to the overpass time of MODIS-AQUA (between $20:00$ and $21:30$ UTC) and OMI (between $20:00$ and $22:00$ UTC) over California. RegCM AOD is the sum of smoke and dust AOD for comparison with MODIS and OMI AOD, also reported in Figure 4 (at 500 and 550 nm, respectively). MODIS and OMI AOD retrievals are limited to cloud-free sky, which restricts the comparisons between RegCM and satellite observations over the Pacific Ocean. To overcome this restriction, we also use the ACAOD product derived from the POLDER and OMI sensors (Jethva et al., 2016; Peers et al., 2015; Torres et al., 2012; Waquet, Cornet, et al., 2013; Waquet, Peers, et al., 2013).

Based on OMI and MODIS retrievals, one can observe that significant AOD are detected by both sensors between 35°N and 40°N , consistently with RegCM. However, Figure 4 also indicates that the regional extent of AOD is not well captured by RegCM for 9–12 July. After 12 July, simulations represent more consistently the location and the magnitude of AOD over this intense biomass-burning source region. During this period, significant AOD are simulated by RegCM, around ~ 1 to 2 (at 550 nm) near smoke sources and between ~ 0.3 to 0.7 in the Pacific outflow. In addition, comparisons between AOD derived from MACC reanalysis and RegCM indicate also large differences, especially between 11 and 14 July (note that MACC reanalysis is daily averaged). We can observe that the regional extent of AOD is generally better reproduced by MACC compared

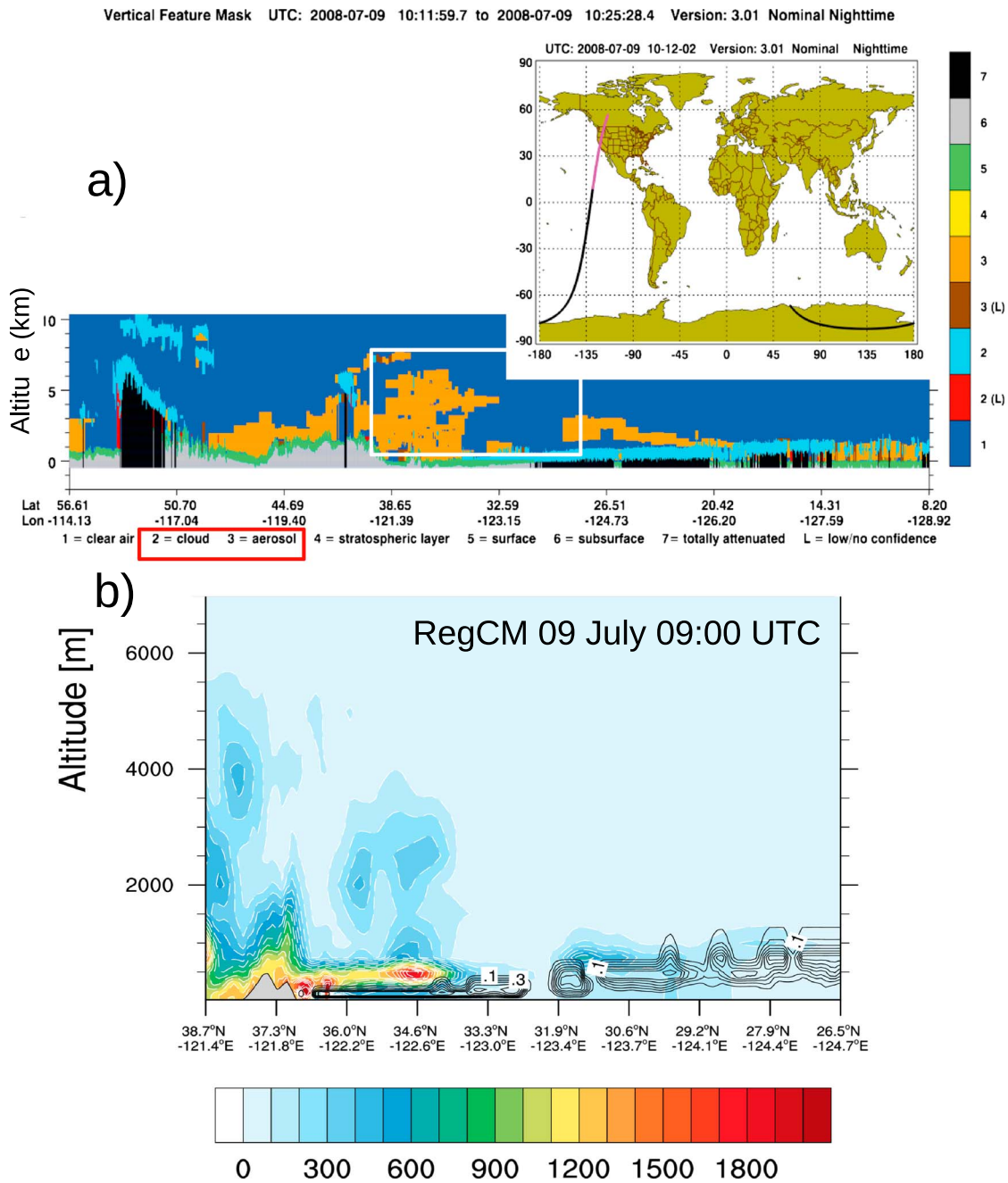


Figure 3. (a) CALIOP vertical profiles obtained for 9 July, showing clouds (light blue color) and aerosols (orange color), and the location of the transect is indicated. (b) The vertical profiles of aerosol accumulation number concentrations (in cm^{-3}) and CF estimated by RegCM is indicated for the similar transect (bottom).

to RegCM especially over land, when compared to satellite AOD retrievals. We can also observe that RegCM captures the intense fires activity at the end of the episode (13 to 14 July). For this period, the model simulates the extreme AOD (~ 1.5 at 550 nm) observed by MODIS over north of California.

Additional comparisons, between OMI, MACC, and RegCM, have been performed over the intense biomass-burning source region detected by MODIS and OMI in Northern California. Both AOD values, averaged over the 120/125°W to 38/42°N domain, are reported in Figure 5. We also report mineral dust AOD for both RegCM and MACC, as well as smoke AOD (RegCM) and anthropogenic (MACC) AOD. First, Figure 5 indicates that the simulated AOD is consistent with OMI observations even if an underestimation is generally observed and

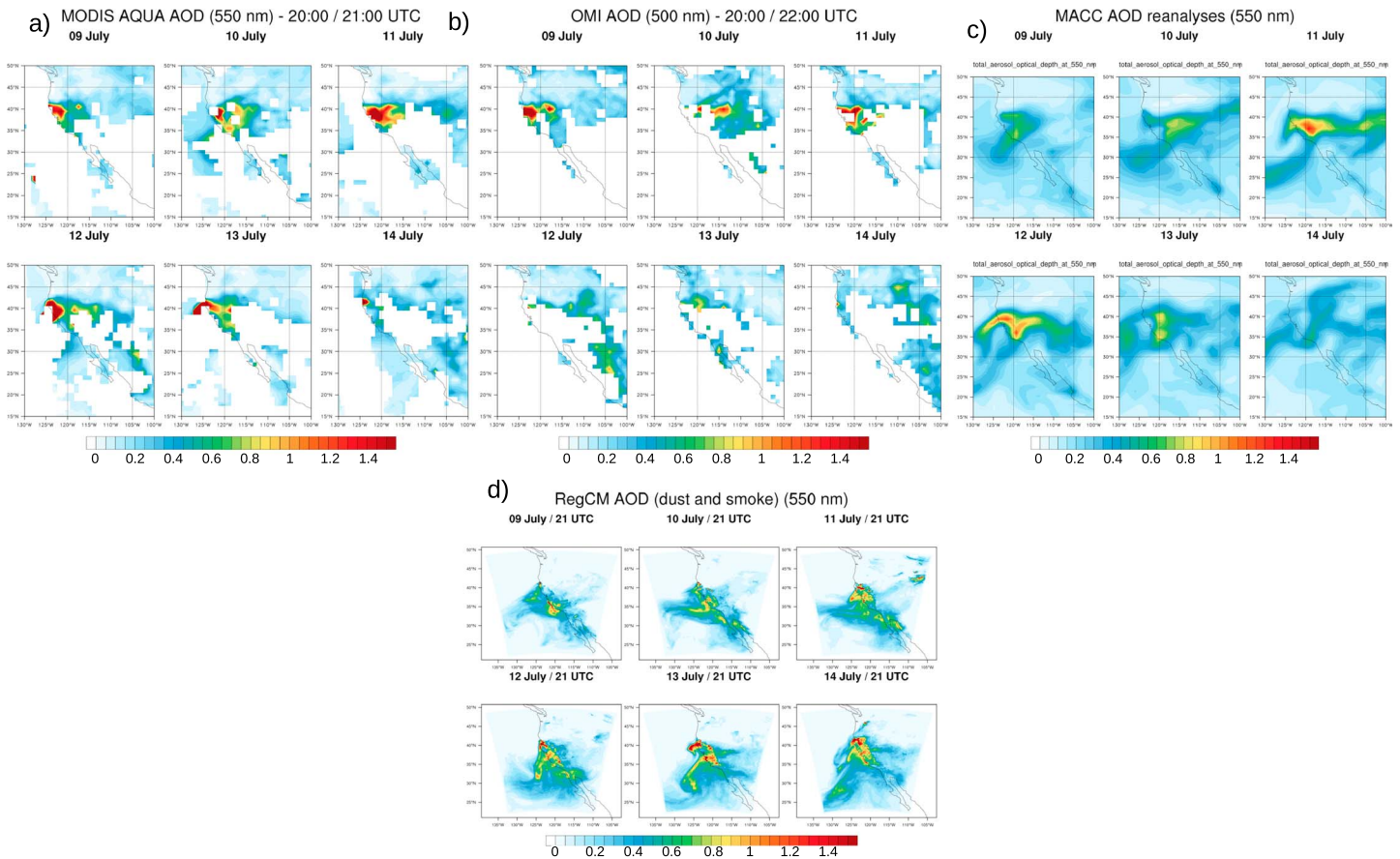


Figure 4. Aerosol optical depth (AOD) retrieved from (a) MODIS, (b) OMI, (c) MACC reanalysis, and (d) RegCM simulations (here at 21 UTC) for the 9 to 14 July period.

characterized by a negative bias of -0.3 over the whole period. For the total AOD, the two maxima detected by OMI (AOD of ~ 1 at 500 nm) are well captured by RegCM; the first (24–29 June) being underestimated by RegCM compared to MACC. At the end of the period (9 to 14 July), a significant increase in AOD is simulated by RegCM, with values reaching ~ 0.75 (14 July), in accordance with OMI observations. However, a delay can be observed in the simulated maximum.

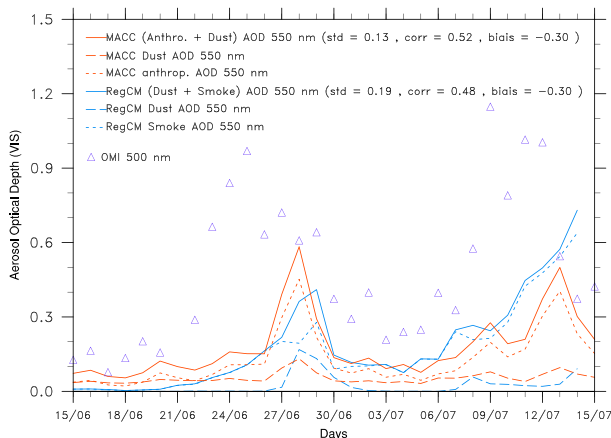


Figure 5. Mean AOD (550 and 500 nm) estimated for the 120–125°W/38–42°N domain, from OMI, RegCM, and MACC. RegCM total AOD and AOD due to smoke and dust are reported (solid and two dashed blue lines) at 21:00 UTC. Total daily MACC AOD and AOD due to dust and anthropogenic particles are reported (solid and two dashed red lines).

In addition, Figure 5 indicates that dust-only AOD is found to be almost similar between MACC and RegCM, showing a contribution of about ~ 0.1 – 0.2 (at 550 nm) for both modeling systems. The RegCM dust AOD is shown to contribute to the total AOD only for the first maxima, while the contribution is low for the second period, with dust AOD ~ 0.05 (at 550 nm). Finally, it should be noted that the temporal correlation is about 0.39 for RegCM for the period of interest. This time delay detected between simulated and observed AOD, especially for the second period (9 to 14 July), could be linked to dynamical errors in the absence of spectral nudging technique in RegCM. The fact that there is no simulated diurnal cycle but only a day to day variability in the prescribed emission could represent another reason explaining the time delay detected between simulated and observed AOD.

4.2.2. Aerosol Optical Depth—Comparisons With AERONET

In addition to satellite observations, we used AOD observations at three different AERONET stations; Trinidad, Monterey, and University of California, Santa Barbara (UCSB) (Santa Barbara, California). Figure 6 reports simulated AOD (every 3 h), the daily MACC AOD reanalyses, MODIS AOD, and instantaneous AERONET (Level 2) observations. The dust AOD is also reported for RegCM and MACC

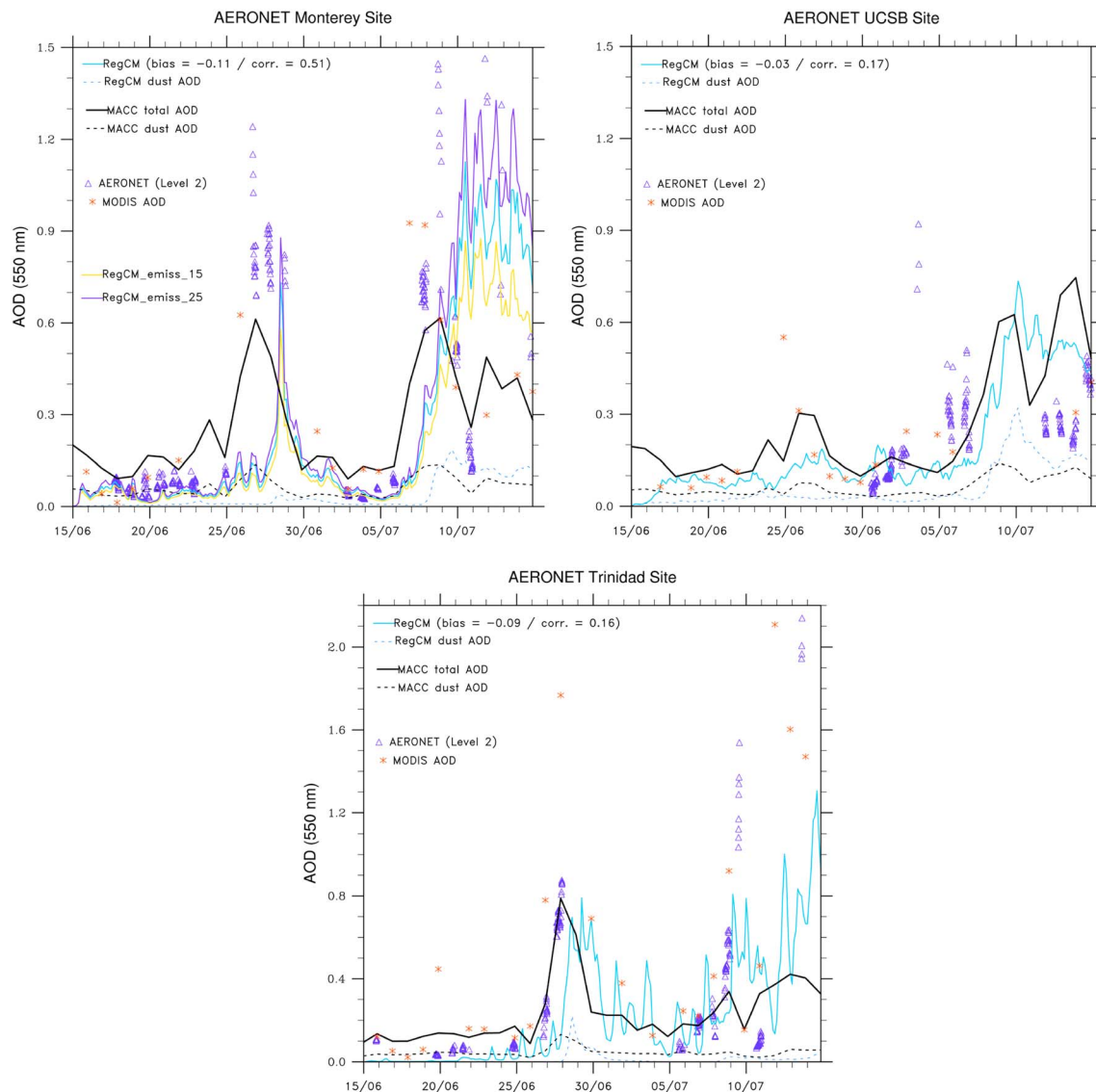


Figure 6. AOD derived at 550 nm at three different locations (Monterey, Trinidad, and UCSB). Instantaneous AERONET (Level 2) AOD data are reported by the blue triangles and the MODIS AOD (550 nm) by the red stars. The total and dust RegCM AOD are reported by solid and dotted cyan lines, respectively. MACC AOD for total (solid) and dust (dotted) aerosols are also reported (at 550 nm) by black lines. The bias and temporal correlation are only reported for RegCM (outputs every 3 h) based on phased (in time) AERONET AOD. For the Monterey AERONET site, the total RegCM AOD calculated with the two tests on emissions are indicated with the yellow and purple lines.

reanalysis. Concerning the Monterey station, the two distinct periods characterized by significant observed AOD are well captured by RegCM even if the duration of the first event (from 25 to 29 June) is shorter than observed in AERONET and MODIS data. For this specific period, we clearly observe that MACC reanalysis better represent the length of this episode, including a more pronounced contribution of dust AOD (~0.1–0.15 at 550 nm), which is totally absent in RegCM. The second period (8 to 15 July) is reasonably well captured by RegCM, in terms of intensity and duration, even if some low AOD detected by AERONET (~0.1–0.2) and MODIS (~0.3–0.4) between 9 and 11 July are significantly overestimated by RegCM. Figure 6 indicates that simulated AOD for 10–11 July are about ~0.8–1.0 (at 550 nm). For 8 to 15 July, MACC data generally underestimate AERONET AOD even if the timing, especially in the AOD increase, is better captured at the beginning of the smoke event (7–8 July) compared to RegCM.

For the UCSB (34.41°N/119.8°W) station, Figure 6 shows that the range of AERONET and MODIS AOD (0.1 to 0.6, at 550 nm) is well represented by RegCM, even if an overestimation clearly appears for 9 to 15 July. Figure 6 also

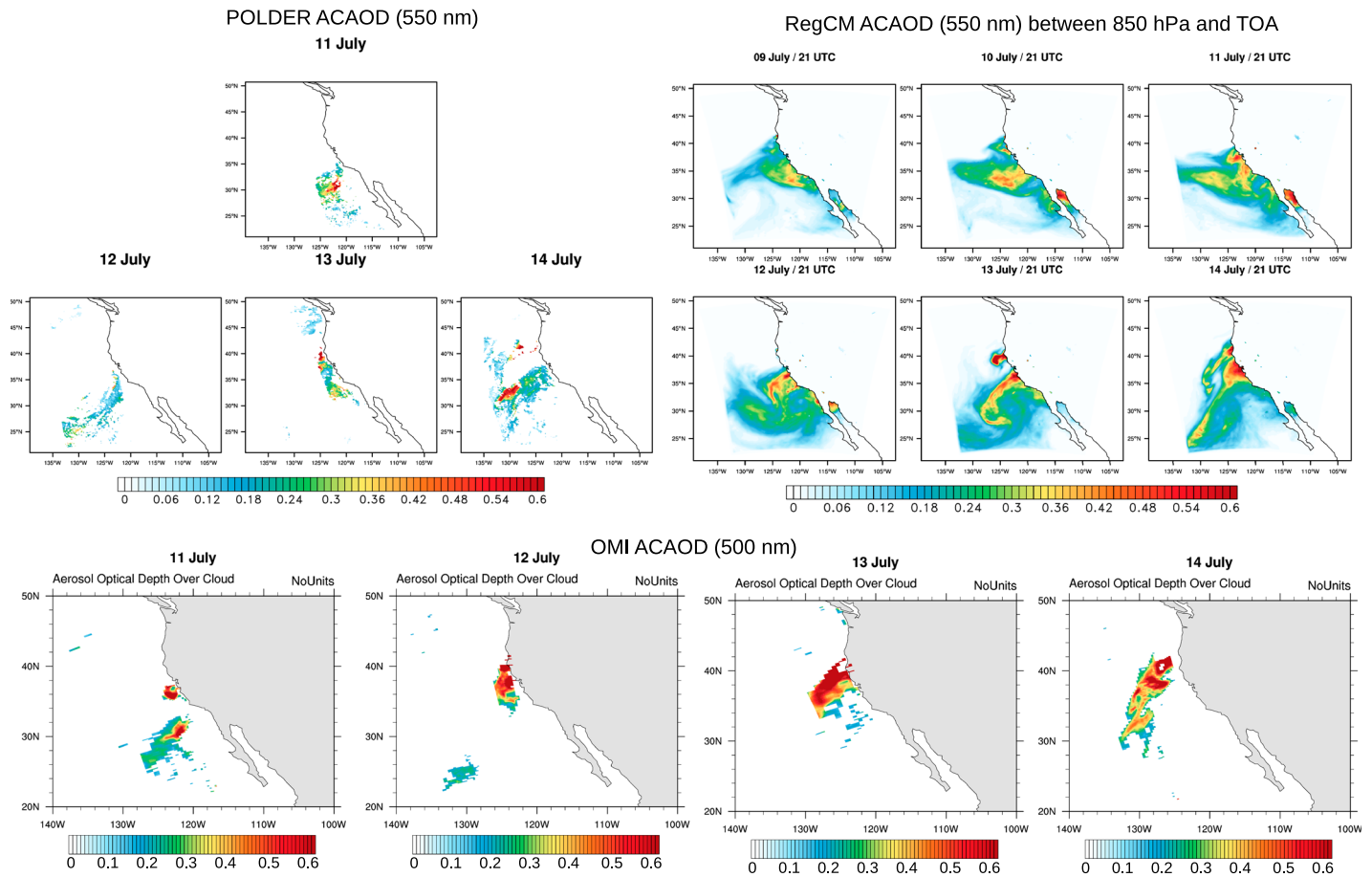


Figure 7. ACAOD estimated from (top left) POLDER (11 to 14 July), (bottom row) OMI (11 to 14 July), and (top right) RegCM (9 to 14 July).

indicates that RegCM is able to capture the temporal variability of AOD, especially the increase observed between 7 and 13 July. It should also be noted that the RegCM dust AOD is important ($AOD \sim 0.15\text{--}0.3$, at 550 nm) for 10 to 14 July. Results obtained at the Trinidad ($41.05^\circ\text{N}/124.15^\circ\text{W}$) station indicate similar conclusions. Indeed, the magnitude of the first AOD maxima is well represented by RegCM and MACC, with a better temporal timing in MACC data. For the second period of time (8 to 15 July), RegCM captures the significant increase in AOD observed by AERONET and MODIS (up to ~ 2 at 550 nm) without reaching the extreme observed values. RegCM does a better job in capturing the decrease in AOD occurring around 11–12 July. For this second period, RegCM simulates the large observed (MODIS and AERONET) AOD with a better agreement than MACC. For this specific station, it should be mentioned that the contribution of other aerosols to the total AOD is found to be low (except RegCM dust AOD for 28–29 June). The comparisons between RegCM and AERONET data shows reasonable performance of the model to simulate the magnitude of AOD during this smoke event despite a general underestimation (negative mean bias ranging from -0.03 to -0.11 , at 550 nm).

4.2.3. Above-Cloud AOD

Figure 7 reports the ACAOD derived from POLDER (top left), RegCM (top right), and OMI (bottom row). RegCM ACAOD has been estimated from 850 hPa to the top of the model to be vertically consistent with satellite data and at 21:00 UTC (time of POLDER overpasses). As reported in Figure 7, the exploitable period is 11 to 14 July when POLDER data are available. The 13–14 July period provides information on smoke ACAOD near sources and close to the Californian coast, while 11, 12, and 14 July allow some comparisons with simulations during the transport of smoke to the Ocean. For 13 and 14 July, the significant ACAOD (~ 0.6) observed by POLDER near the coast (at $\sim 40^\circ\text{N}$) are realistically reproduced by RegCM in terms of magnitude and regional extent. For 14 July and at these latitudes, Figure 7 shows that RegCM slightly underestimates ACAOD during the transport with values around ~ 0.4 , compared to POLDER (~ 0.6). For these two days, a second biomass-burning plume located southern ($\sim 35^\circ\text{N}$) is simulated by RegCM, which is absent in POLDER observations.

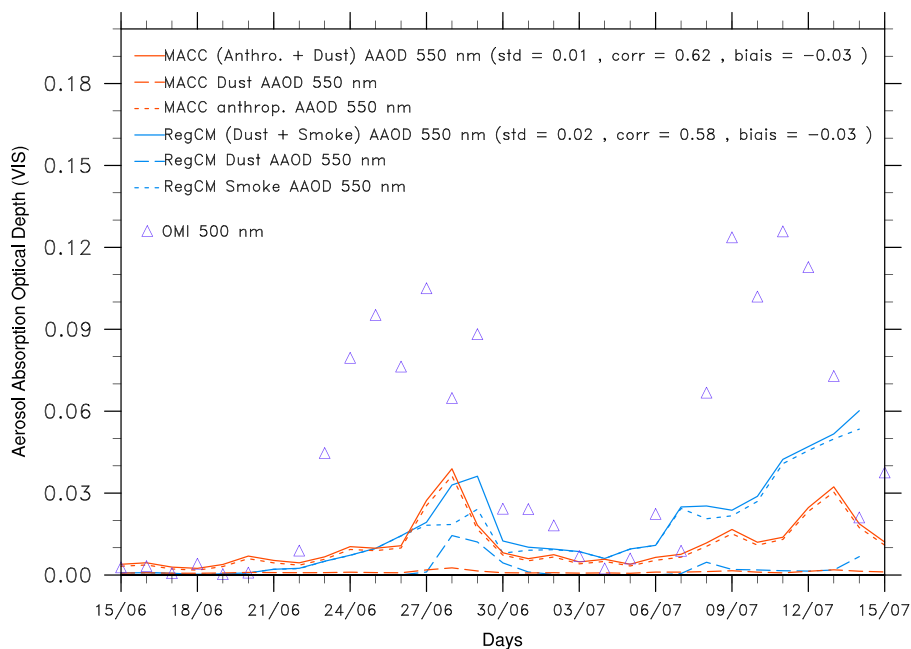


Figure 8. Mean AAOD (550 and 500 nm) for the 120–125°W/38–42°N domain estimated by OMI, RegCM, and MACC. RegCM total AAOD and AAOD due to smoke and dust aerosols are reported by solid, dotted, and dashed blue lines, respectively, at 21:00 UTC. Daily total MACC AAOD and AAOD due to anthropogenic and dust particles are reported by solid, dotted, and dashed red lines.

During 11, 12, and 14 July, POLDER indicates transported smoke plumes characterized by ACAOD of $\sim 0.1\text{--}0.4$ (for 12 July) and $\sim 0.2\text{--}0.6$ (for 12 and 14 July). Figure 7 shows that the values of ACAOD is well respected by RegCM for 12 July during the transport (ACAOD around $\sim 0.2\text{--}0.3$), while a slight underestimation is observed for 11 July compared to POLDER. For 14 July, the calculated ACAOD by RegCM ($\sim 0.3\text{--}0.4$) is underestimated compared to POLDER (~ 0.6) data. In addition, for this case, RegCM ACAOD is located to the south of the plume compared to POLDER observations.

The comparisons of OMI and POLDER ACOAD retrievals clearly reinforce the presence of significant aerosol concentration above the cloud deck due to biomass-burning emission. As observed by POLDER, OMI shows also significant ACAOD (values larger than 0.6 at 550 nm) above the Pacific Ocean. We can also note an interesting consistency between the two sensors for 13 July near the coast and during the transport for 11 and 14 July, even if some differences in the magnitude of ACAOD are also observed.

4.2.4. Aerosol Absorbing Optical Depth

In this section, AAOD and SSA are analyzed as well as their spectral dependence. As already performed for AOD, we first compared AAOD derived from OMI (at 500 nm) with RegCM simulations (at 21:00 UTC) for the whole domain and for the 9 to 14 July period. These comparisons are illustrated in Figure S6 (supporting information). The results indicate that the location of AAOD maxima is well represented by RegCM, but the regional extent and its magnitude are clearly underestimated, except for 12, 13, and 14 July. In particular, the significant AAOD derived from OMI over land for 9 and 10 July is totally absent in the RegCM simulations with AAOD between 0.05 to 0.1 (at 550 nm).

Additionally, we have conducted comparisons between OMI, RegCM, and MACC AAOD for the same box as defined for AOD (section 4.2.1) where a maximum of AAOD is detected. The results are presented in Figure 8, where the same variables as presented in Figure 5 are reported but for AAOD. As for AOD, the first maxima ($\sim 0.05\text{--}0.08$ at 500 nm) in AAOD observed from OMI (24 to 29 June) is well detected by RegCM and MACC, but both modeling systems underestimate its magnitude. For this specific period, it should be noted that RegCM indicates a moderate contribution of dust AAOD (~ 0.015 at 550 nm) to the total AAOD, which is absent in MACC reanalysis. For the second smoke episode and even if the AAOD simulated by RegCM increases for this period (8 to 15 July), the maxima observed from OMI (~ 0.12 at 500 nm) are not reproduced by RegCM (maxima of ~ 0.06 at 550 nm). For this period, RegCM AAOD is found to be higher than MACC, which simulates AAOD comprising between 0.01 and 0.03 (at 550 nm). It should be mentioned that, for both models, dust AAOD is found to be low during this period. The RegCM underestimate compared to OMI is quantified by a mean negative bias of -0.03 (at 550 nm) for the whole period, which is equal to the one calculated from MACC data.

In addition, we have investigated the AAOD spectral dependence, which is an important optical property for absorbing smoke (Russell et al., 2010). This aspect is generally studied using the absorbing Angström exponent (AAE) calculated between two different wavelengths (Russell et al., 2010). The results (not shown, Figure S7 in the supporting information) indicate the OMI and RegCM AAE estimated in the box (120–125°W/38–42°N) and for the whole period of the simulation. Results indicate higher AAE values for OMI compared to RegCM, when calculated using similar wavelengths (400 and 550 nm). Such comparisons indicate that RegCM AAE is lower than OMI observations, the latter being consistent with values (from 1.42 to 2.07; calculated between 405 and 870 nm) reported by Gyawali et al. (2009) during July 2008 in Reno (Nevada). We obtain similar conclusions when comparing OMI and RegCM AAE with data reported by

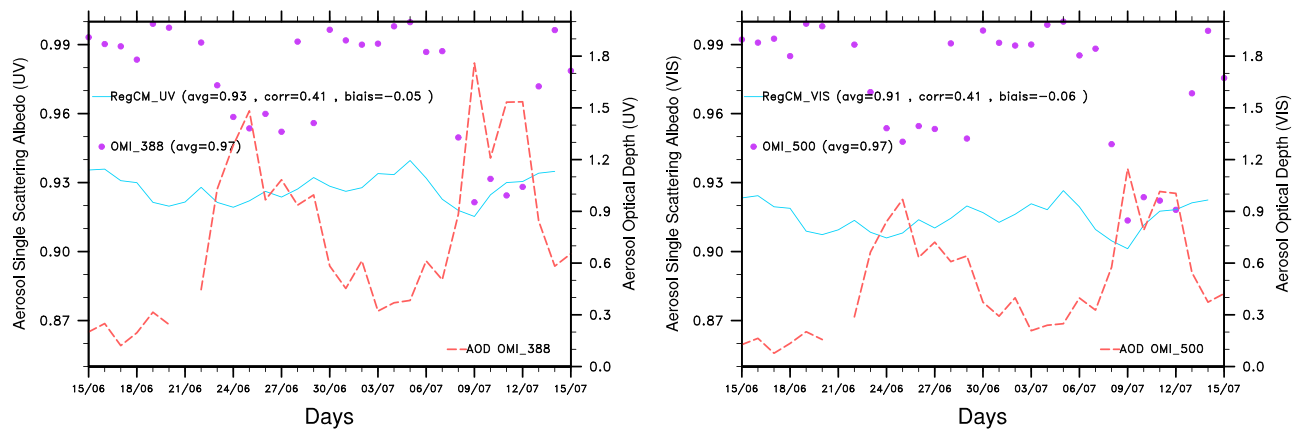


Figure 9. Aerosol SSA estimated in the ultraviolet (UV) and visible (VIS) spectral ranges by RegCM (21:00 UTC) and OMI and averaged over the 121 to 124°W and 38 to 41°N domain. The corresponding OMI AOD are also indicated for both wavelengths (red dashed lines).

Clarke et al. (2007) or Chung et al. (2012), who report AAE comprising between 1.2–2.5 (470–670 nm), and 1.4–2.1 (405–870 nm) for biomass-burning aerosols. This could be due to the absence of specific parameterizations of absorbing properties of brown carbon particles in the present version of RegCM. As such aerosols are able to absorb ultraviolet radiations (Feng et al., 2013), they need to be taken into account. This first analysis indicates that further developments are required, possibly by using more realistic refractive index of smoke in the UV, to improve the spectral dependence of absorbing radiative properties.

4.2.5. Smoke Single Scattering Albedo

Figure S8 (supporting information) represents the instantaneous (21:00 UTC) smoke SSA estimated at 400 and 550 nm by RegCM and for 9 to 14 July. This figure indicates OMI SSA ~ 0.85 – 0.90 (at 500 nm) around 40°N–122°W, especially for 9 and 11 July, consistently with the significant OMI AOD and AAOD due to smoke (Figures 4 and S5). For the rest of the period, OMI SSA is not derived near biomass-burning sources. Over land, OMI indicate higher values ~ 0.95 (at 500 nm), which is likely due to the mixing of smoke with dust particles. For 9 and 11 July in particular, the results indicate that RegCM SSA is in a good accordance with OMI observations near smoke sources with RegCM SSA ~ 0.85 – 0.90 (at 550 nm). Such estimates are found to be also consistent with values reported by Gyawali et al. (2009) who derive SSA at the Nevo station comprising between 0.88 and 0.93 (at 405 nm) during July 2008. Finally, RegCM SSA is increasing, reaching values ~ 0.93 – 0.95 (at 550 nm) when smoke particles are transported over the Pacific Ocean.

We have also evaluated RegCM SSA with OMI observations for the whole period over a specific box (120–125°W/38–42°N) (Figure 9) for UV (left) and VIS (right) spectral ranges. The OMI AOD (red dashed line) is also reported for both wavelengths. This figure indicates clearly the decrease in OMI SSA (for both spectral ranges) for the two periods already identified. For AOD higher than 1 (at 388 nm), OMI SSA is ~ 0.95 – 0.96 (388 nm) for 23–25 June and between ~ 0.92 and 0.95 (388 nm) for 8 to 13 July corresponding to extreme AOD (~ 1.5 at 388 nm). Outside of these two periods, OMI SSA is nearly 1 associated with a weak day to day variability. Similar conclusions are obtained at 500 nm with lowest values compared to 388 nm. Concerning RegCM calculations, Figure 9 indicates that daily SSA comprise between 0.91–0.94 (at 400 nm) and 0.90–0.93 (at 550 nm) for the whole period and the day to day variability is less pronounced than OMI retrievals. For both spectral ranges, RegCM correctly simulates (SSA ~ 0.92 – 0.93 at 380 nm) the magnitude of OMI SSA (~ 0.91 – 0.92 at 388 nm) for the second episode (8 to 13 July), while a negative bias is observed during the first event. When calculated over the whole period, a mean negative bias of -0.06 (UV) and -0.05 (VIS) is estimated between RegCM and OMI SSA, mainly due to the significant bias observed outside of the two smoky periods.

4.2.6. Above-Cloud Single Scattering Albedo

In order to study smoke absorbing properties during the transport, we have used the above-cloud single scattering albedo (ACSSA) products recently developed for the POLDER sensor (Peers et al., 2015; Waquet, Cornet, et al., 2013; Waquet, Peers, et al., 2013). The results (not shown, Figure S9 in the supporting information) indicate ACSSA (550 nm) from POLDER and RegCM, respectively, for 13 and 14 July. For 13 July, POLDER provides

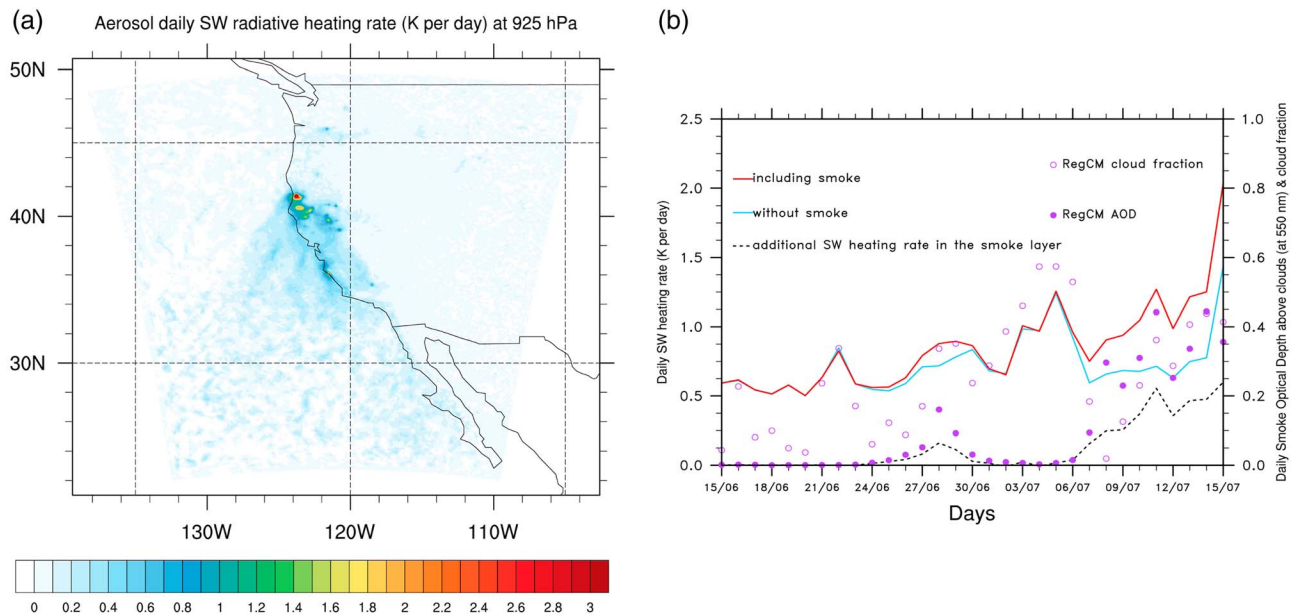


Figure 10. Daily SW heating rate (in °K/d) exerted by absorbing smoke particles at (a) 925 hPa averaged for the 9 to 14 July period and (b) over the 123–126°W/37–40°N domain. SW heating rate calculated by RegCM is reported for simulations including or not smoke (red and blue lines). The daily heating rate directly due to smoke is represented by the dotted black line. The daily RegCM AOD (at 550 nm) and CF are also included.

estimates of ACSA near the Californian coast, characterized by a large variability with values mostly ranging between 0.90 and 0.95 (at 550 nm). Some isolated values reaching nearly 1 are also derived by POLDER further from the Californian coast for this day. The lower values (~0.90–0.92) are derived near the coast. For the same event, RegCM simulates realistic values of ACSA (at 550 nm) comprising between 0.91 and 0.93, associated with low variability compared to POLDER retrievals. We observe also the absence of values of ~1 for ACSA calculated by RegCM during the transport. On 14 July, POLDER data indicate clearly an increase of ACSA in the outflow with values around ~0.96–0.98 for most of the detected pixels. Absorbing smoke (ACSSA ~0.90–0.92) is detected near the coast and curiously for some isolated pixels away from the coast (for longitudes of 130–135°W), maybe due to the recirculation of smoke. The calculated ACSA by RegCM is found to be similar to that of 13 July, and this case underlines a clear overestimate of ACSA during the transport by RegCM. Indeed, the gradient in ACSA detected by POLDER during the transport is absent in RegCM calculations, which could be due to the dependence of this optical parameter to grid cell relative humidity as implemented in the model or to a poorly representation of SOA aerosols in the current version.

4.3. Smoke SW Radiative Heating and TOA DRF

4.3.1. SW Heating Rate

Figure 10a displays the daily mean simulated SW radiative heating rate only due to absorbing smoke and averaged for the 9 to 14 July period (at 925 hPa). The results indicate significant SW heating within the smoke plume advected over the Pacific Ocean and near biomass-burning sources. Near sources, the additional SW heating is about ~2–3°K/d and decreases during the transport to ~0.5–1.5°K by day. Contrary to other radiative parameters, the SW heating rate is not derived by satellites and not provided by reanalyses to our knowledge. Hence, in order to evaluate the simulated SW heating, we used the study of Wilcox (2010), who provides useful estimates of SW heating attributable to smoke for different cloud fractions established over the Namibian region. In this work, the mean (averaged within the smoke plume) SW heating ranges between 1.5 and nearly 2°K/d for smoke AOD of 1.0, in cloud-free conditions, and for CF of 1 (Wilcox, 2010, Figure 3). To compare with those estimates, we reported in Figure 10b the SW heating rate averaged over 123–126°W/37–40°N within the smoke layer located above clouds. We also indicated (Figure 10b) the smoke ACAOD and the CF averaged between 1,010 and 950 hPa. Although the ACAOD calculated in our situation does not reach those reported by Wilcox (2010), we can observe ACAOD ~0.5 (at 550 nm) for the 8 to 15 July period with CF comprising between 0.2 and 0.5. In the absence of smoke, the (diurnal mean) SW heating rate is about ~0.5°K d⁻¹. When smoke is included in the simulations, the SW heating increases and comprises between

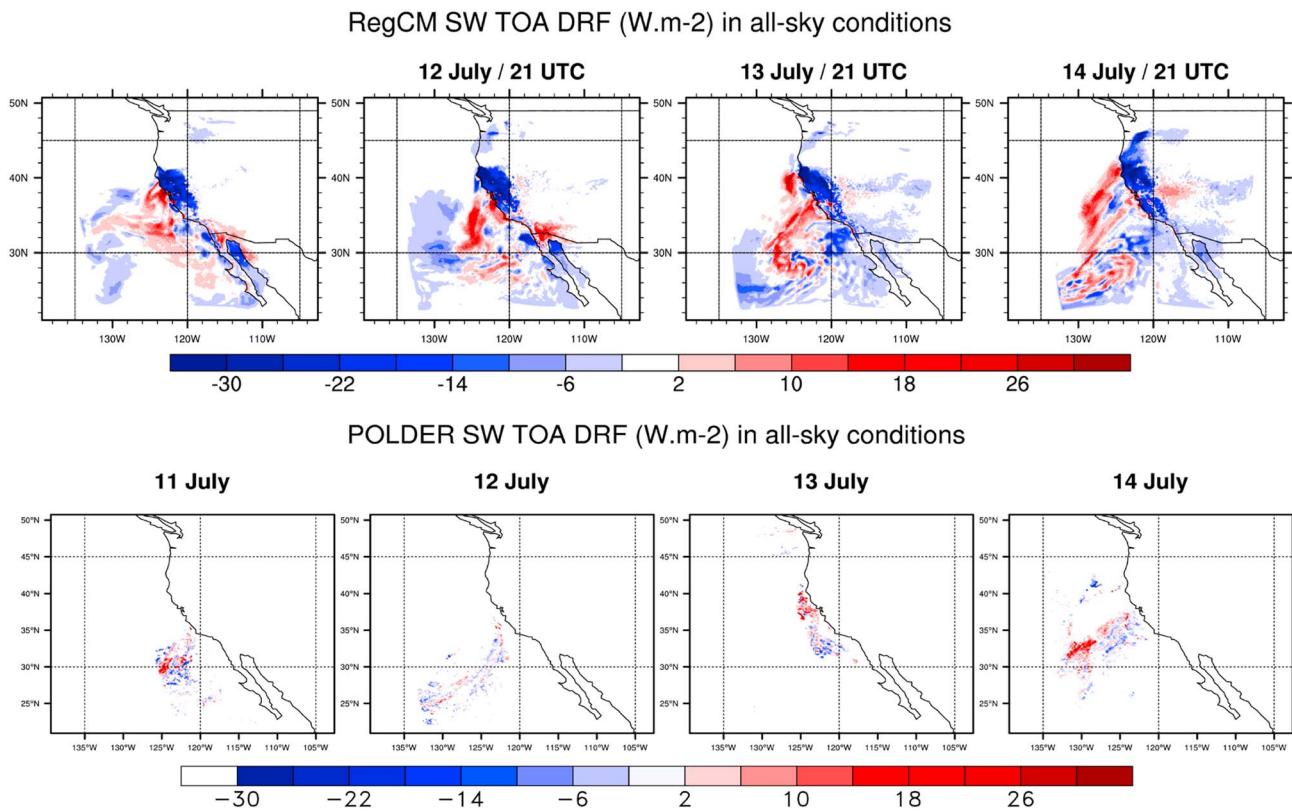


Figure 11. Direct radiative forcing (DRF) estimated at TOA in the shortwave (SW) from (top row) RegCM at 21:00 UTC and (bottom row) POLDER for 11–14 July and in all-sky conditions.

0.7 and 1.2K d^{-1} . Such values are found to be slightly lower than those reported by Wilcox (2010), for smoke ACAOD ~ 0.4 . Indeed, Wilcox (2010) has indicated that the SW heating is going from 1K d^{-1} in the absence of smoke to values comprising between 1.5 and 2K d^{-1} within the smoke layer, located between 600 and 700 hPa pressure levels. Such values are found to be consistent with those reported in Figure 10b, with a value of SW heating around 0.5K d^{-1} due to smoke. The slightly lower warming observed in our case may be due to smoke SSA, which is higher in our study (0.95 at 550 nm) compared to Wilcox (2010) (0.89 at 550 nm).

4.3.2. TOA SW Direct Radiative Forcing

In this section, different estimates of the SW TOA DRF in all-sky conditions have been compared, using POLDER and RegCM data for the 11 to 14 July period. Figure 11 indicates the instantaneous RegCM (21:00 UTC) (top) and POLDER (bottom) estimates. It should be recalled here that DRF from POLDER is not a satellite estimate since it is based on radiative transfer calculations. For RegCM and MACC, the direct radiative forcing is estimated by using the difference of two simulations including or not aerosols, all other variables being the same. The differences in the net SW radiative fluxes at TOA (without any change in the meteorological fields) are used to estimate the direct radiative forcing.

The results indicate that the SW DRF simulated at TOA by RegCM can be both negative or positive during the transport of smoke over the Pacific Ocean (the values reported at 21:00 UTC being logically higher than the diurnally averaged), while the SW TOA forcing over the continent is negative. Figure 11 indicates that RegCM is able to simulate the change of sign in the SW DRF at TOA when absorbing smoke is advected over Sc. The positive values of the TOA forcing estimated by RegCM can peak to $+20\text{--}25\text{W m}^{-2}$, which is found to be consistent with the values reported by DeGraaf et al. (2014) over the Namibian region, who indicated TOA forcings between $+10$ and $+40\text{W m}^{-2}$.

As for RegCM calculations, POLDER estimates also indicate positive and negative DRF at TOA over the ocean. Significant positive values are clearly observed for 11, 13, and 14 July with forcings being locally about $+5$ to $+15\text{W m}^{-2}$, especially near the coast for 13 July and along the transport for 11 and 14 July, consistently with the significant ACAOD detected by POLDER for these days. An interesting result is the two opposite forcings

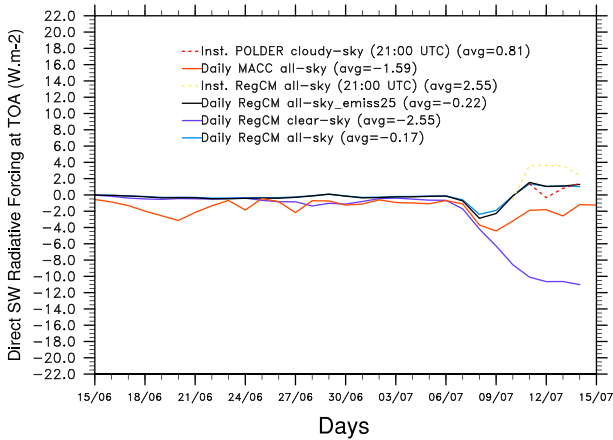


Figure 12. Averaged SW direct radiative forcing at TOA over the domain 118–130°W/30–38°N from POLDER (red line), RegCM (21:00 UTC, dashed blue line), RegCM (daily, in clear-sky and all-sky conditions; solid and dashed blue lines and solid black line for POM to OC ratio of 2.5), and MACC reanalysis (yellow line).

derived from POLDER for two distinct smoke plumes located at 32–34°N and 40–42°N, which are characterized by positive and negative forcings, respectively. This difference in the sign could be due to the difference in the optical (COD) and microphysical (CER) properties of Sc located under the absorbing smoke (Figure 3) and to the absorbing properties of smoke. ACSSA derived from POLDER indicate highest values (~1 at 550 nm) at 40–42°N, compared to those (0.90–0.96 at 550 nm) detected for the second plume (32–34°N). Hence, for 14 July, the two smoke plumes transported over the ocean lead to different SW direct forcing at TOA, mostly negative for the first event and positive for the second. This underlines the complexity of simulating the sign itself of transported smoke over Sc regions, due to the variability of biomass-burning radiative properties, which could be due to the type of burned vegetation and/or modification during the transport (changes with the relative humidity). During 13 July, the significant ACAOD observed from POLDER (Figure 7) associated with ACSSA comprising between 0.90 and 0.95 (at 550 nm) near the coast leads to a positive direct forcing at TOA peaking at $+20 \text{ W m}^{-2}$.

The results reported in Figure 11 indicate that the RegCM DRF estimates are found to be consistent with POLDER observations. For 13 July, when smoke is mostly observed near the coast, the positive TOA DRF detected by POLDER is reasonably well estimated by RegCM at 40°N, in terms of location and magnitude. However, and for this day, the significant positive DRF calculated by RegCM at latitudes lower than 38°N are not detected by POLDER. This is due to the differences in ACAOD for this specific event. Indeed, as shown in Figure 7, the second smoke plume (located at latitudes lower than 38°N) simulated by RegCM is absent from POLDER

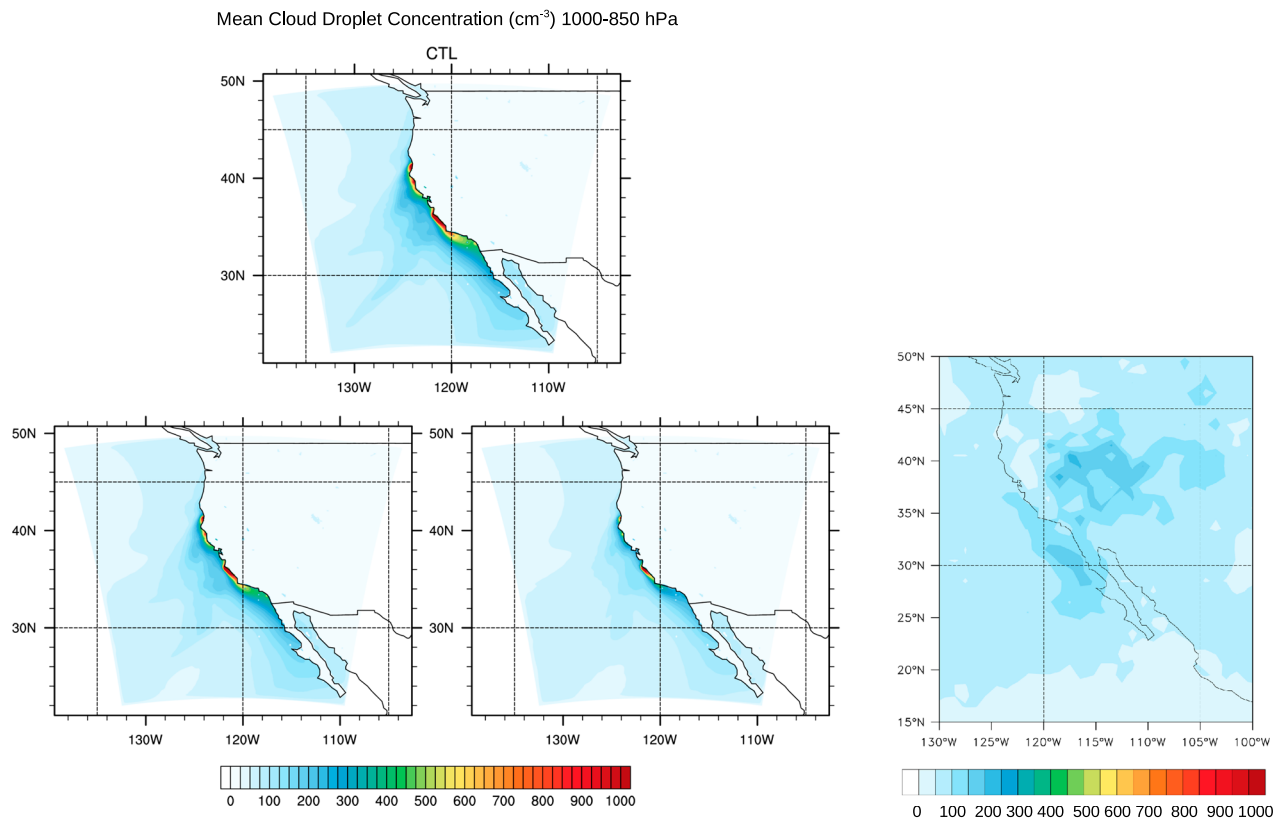


Figure 13. Cloud droplet number concentrations (CDNC) estimated by RegCM for the whole period and for 1,010–850 hPa using three different assumptions on the smoke hygroscopic properties: (top) 75% (control CTL simulation), (bottom left) 60%, and (bottom middle) 50%. (bottom right) The CDNC derived from MODIS for the whole period is also indicated.

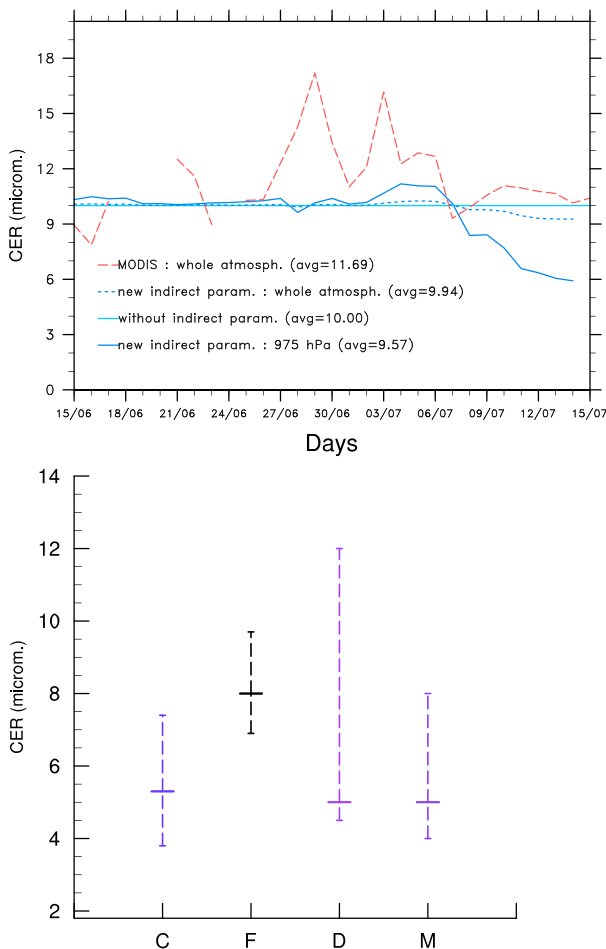


Figure 14. (top) Mean (over the 120–125°W/30–40°N domain) liquid cloud effective radius (CER) (μm) estimated from RegCM simulations (at 975 hPa and for the whole atmospheric column) including (or not) the new parameterization and MODIS observations. (bottom) The CER observed for Sc during experimental campaigns conducted over the Californian region (listed in Table 3) are also indicated, including the maximum and minimum values.

observations. For 14 July, the positive DRF detected by POLDER above the oceans ($\sim 32^\circ\text{N}/130^\circ\text{W}$) is also well reproduced by RegCM. In this case, DRF is approximately $+20 \text{ W m}^{-2}$ for both RegCM and POLDER estimates.

Additionally, we have calculated the mean SW DRF over the following domain: 120° to $130^\circ\text{W}/30^\circ$ to 38°N . The results are reported in Figure 12 for the MACC reanalysis (daily value), RegCM (instantaneous at 21:00 UTC and daily), and POLDER (21:00 UTC). The RegCM instantaneous estimates (dashed blue) are only indicated for the period corresponding to POLDER observations. We first observe that the daily mean DRF estimated by RegCM ranges from -2.55 W m^{-2} in clear-sky conditions to -0.17 W m^{-2} in all-sky conditions. The mean SW DRF obtained by using a POM to OC ratio of 2.5 is also reported in Figure 12 and indicates a value of -0.22 W m^{-2} in all-sky conditions. When calculated at 21:00 UTC (corresponding to the time of POLDER overpasses), the RegCM instantaneous DRF is found to be positive ($+2.5 \text{ W m}^{-2}$) in all-sky conditions, in a better accordance with POLDER estimates. However, the mean RegCM value is found to be higher than the averaged DRF obtained with POLDER ($+0.81 \text{ W m}^{-2}$) observations during the 11–14 July period. Based on these comparisons, combining RegCM simulations with the original POLDER products (Peers et al., 2015), this analysis demonstrate that RegCM is able to simulate the positive DRF exerted by absorbing aerosols in case of biomass burning transported over marine Sc. However, some differences appear in the magnitude of the forcing between RegCM and POLDER which could be due to difference in ACAOD, ACSSA and cloud properties.

4.4. Smoke First Indirect Radiative Effect

4.4.1. Cloud Droplet Number Concentration

As mentioned previously, a relationship was implemented to estimate the first indirect effect of smoke aerosols. The calculated CDNC (in cm^{-3}) over the whole period and averaged between 1,010 and 850 hPa, as well as MODIS retrievals, is shown in Figure 13. The results obtained from the two sensitivity tests are also indicated. This figure indicates that CDNC are in the order of magnitude of about $400\text{--}1,000 \text{ cm}^{-3}$ near the coast and $\sim 200\text{--}400 \text{ cm}^{-3}$ during the transport for the control (CTL) simulation. The extreme values of CDNC ($\sim 1,000 \text{ cm}^{-3}$) are obtained near biomass-burning sources. The results obtained from the two sensitivity tests show that the CDNC concentration is considerably reduced, by about 100 to 300 cm^{-3} depending on the hygroscopicity of smoke. For example, the simulation using the hygroscopic factor of 50% indicates CDNC around $200\text{--}400 \text{ cm}^{-3}$ for most of the domain, which is in a good agreement with the values obtained from MODIS by Painemal and Minnis (2012) over the Californian region. We also report in Figure 13 the mean MODIS CDNC (estimated from equation 5 of Painemal and Minnis (2012)) for the whole period, indicating that, except near the coast, the CDNC is well reproduced by RegCM, especially for the test using the hygroscopicity of 50%, with values around $200\text{--}300 \text{ cm}^{-3}$. This highlights the important sensitivity of estimated CDNC to the hygroscopic properties of smoke and could explain the larger values of calculated CDNC compared to the available literature over this region, as presented below.

Indeed, over the Californian region, comparisons with published values show that CDNC estimated by RegCM are generally higher than in situ surface observations. As an example, King et al. (1993) and Twohy et al. (2005) reported values of about $\sim 100\text{--}400 \text{ cm}^{-3}$ and $\sim 50\text{--}300 \text{ cm}^{-3}$, respectively. In addition, McComiskey et al. (2009) have reported CDNC ranging from 200 to 800 cm^{-3} during the MASRAD campaign at Point Reyes. The authors indicate that CDNC retrievals could be unstable due to the use of ground-based instrument with different field of view. Obviously, the differences between simulated and referenced CDNC could be due to disparity in the intensity of smoke sources. Compared to intense smoke events occurring in Brazil, the RegCM estimates are found to be consistent with those (CDNC concentrations from 100 to $1,400 \text{ cm}^{-3}$) reported by Reid and Hobbs (1998) for biomass-burning aerosols.

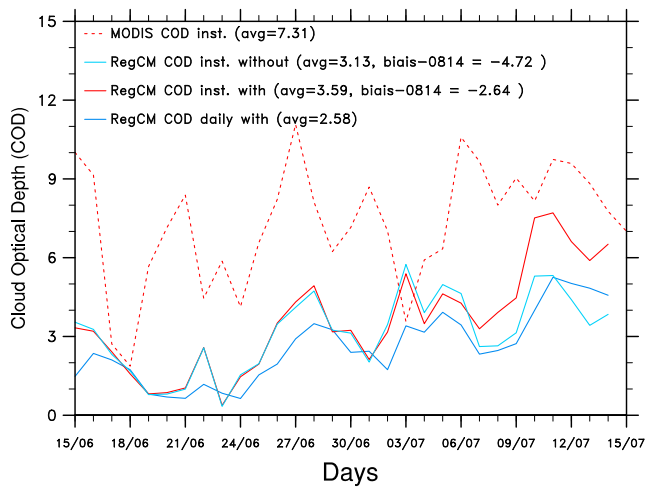


Figure 15. COD estimated from RegCM and MODIS. RegCM daily mean and instantaneous (21:00 UTC) including the parameterization and without the parameterization are indicated by solid dark blue, red solid, and solid light blue lines, respectively. The MODIS COD is indicated by the dashed red line. The spectral range for estimated COD are 0.69–1.19 μm and 0.66–1.24 μm , for RegCM and MODIS, respectively. Averaged values are indicated for the whole period, while the bias between RegCM and MODIS are calculated for the RegCM instantaneous estimates only and for the 8 to 14 July period.

4.4.2. Cloud Effective Radius

The calculated CDNC is used to estimate CER using equation (1). As for CDNC, the RegCM-calculated CER is compared with referenced values only for Sc and over the Californian region (Table 2). In addition, this analysis includes comparisons with CER derived from MODIS (Level 2 product) for 10, 12, and 13 July (not shown, Figure S10 in the supporting information) and for the whole period (Figure S11). Results for 10, 12, and 13 July indicate that near the coast, the CER derived by MODIS could reach values $\sim 6\text{--}7\ \mu\text{m}$, in agreement with RegCM estimates. Some low values (CER $\sim 6\text{--}7\ \mu\text{m}$) are also detected by MODIS away for the coast, in a similar manner to RegCM within the smoke plume. However, the result indicates also some differences in the regional pattern of CER which could be due to bias in the meteorological fields simulated by RegCM (possibly due to the absence of spectral nudging in our simulation).

In parallel, Figure 14 indicates the mean RegCM CER (averaged over box $120^{\circ}\text{--}125^{\circ}\text{W}/30^{\circ}\text{--}40^{\circ}\text{N}$ at 975 hPa) for the whole atmospheric column and including the indirect parameterization. The calculated CER at 975 hPa is reported in Figure 14 as well as the fixed value used without the indirect parameterization. In addition, Figure 14 (bottom) reports the different referenced CER values obtained from in situ observations and for Sc for the different experiments (Table 2).

First, we can observe the decrease of CER simulated by RegCM for the period from 8 to 14 July, when the smoke concentration increases. During this period,

CER is going from $\sim 10\text{--}11\ \mu\text{m}$ (6–7 July) to $\sim 6\ \mu\text{m}$ (14 July) at 975 hPa (the decrease in CER is less pronounced for the RegCM whole atmospheric estimates: from $10\ \mu\text{m}$ to $9.5\ \mu\text{m}$). Even if the CER variability is not captured by the model, the decrease in CER is also observed from MODIS data, showing that CER is passing from $12\text{--}17\ \mu\text{m}$ (27 June to 06 July) to $10\text{--}11\ \mu\text{m}$ (8–15 July). It should be recalled here that the bias between MODIS and RegCM CER could be due, in part, to the impact of above-cloud absorbing smoke aerosols on the MODIS retrievals of cloud properties (Meyer et al., 2015). Although this does not represent a real assessment of the parameterization, Figure 14 (bottom) underlines that the simulated CER (for the period characterized by significant smoke concentration) is in the range of in situ observations, which comprise between 5 and $8\ \mu\text{m}$ for Sc. For example, and in the case of the MASRAD experiment (McComiskey et al., 2009), which is characterized by important CDNC concentrations, CER observed at Point Reyes (California) comprise between 4 and $8\ \mu\text{m}$ and are well within the range of RegCM estimates (from 6 to $8\ \mu\text{m}$). The only real CER observations available during this period were obtained from MODIS sensor and revealed large differences in CER. Even if the decrease of CER observed by MODIS for 8 to 15 July is consistent with RegCM simulations, there is clearly a discrepancy between the absolute values of CER obtained from simulations and from observations (Figure 14, top). However, Twohy et al. (2005), who compared MODIS data with in situ aircraft observations for nine Sc over the Eastern Pacific Ocean, in the framework of the Dynamics and Chemistry of Marine Stratocumulus-II (DYCOMS-II) experiment, indicate that the magnitudes of the MODIS CER are also much higher than measured in situ values ($14.5\ \mu\text{m}$ from MODIS versus $7.6\ \mu\text{m}$ from *in situ*). More recently, Noble and Hudson (2015) reported similar differences between in situ observed and MODIS CER over northeastern Pacific region for Sc. Based on the comparison with MODIS data and different published values over the Californian region, it is shown that RegCM is able to simulate the order of magnitude of CER in a realistic way for marine Sc polluted by biomass-burning aerosols, even if some limitations are underlined.

4.4.3. Implications for Cloud Optical Depth and SW Radiative Fluxes at TOA

In this last section, the changes in optical properties of clouds (COD) and the net SW radiations at TOA are analyzed using two simulations. The first simulation uses the developed indirect parametrization, and the second is realized without activating it. RegCM simulations and MODIS observations have been studied over the $120\text{--}125^{\circ}\text{W}/30\text{--}40^{\circ}\text{N}$ domain. It should be noted that the difference in the SW net radiative fluxes at TOA between both simulations does not represent rigorously the so-called indirect radiative forcing, which is not diagnosed in the present version of RegCM. Here we rather evaluate the radiative perturbations at TOA induced by smoke on Sc using the difference in the net SW fluxes between two RegCM simulations.

In terms of cloud optical properties, Figure 15 shows that the RegCM COD is generally lower than MODIS COD observations for the studied period, which could be due to the liquid water content and microphysical properties of Sc. The objective here is not to analyze the absolute bias between simulated and observed COD but to compare its relative evolution occurring during the smoke event. Furthermore, it should be noted that absorbing aerosols residing above clouds can lead to important biased retrievals of COD, with errors on the order of 10–20% (Haywood et al., 2004). When averaged over the whole period, the mean COD is about ~ 7 for MODIS and between ~ 2 and 3 for the different RegCM estimates for similar spectral ranges ($0.69\text{--}1.19\ \mu\text{m}$ and $0.66\text{--}1.24\ \mu\text{m}$, for RegCM and MODIS, respectively). Figure 15 also illustrates the increase of the COD between 9 and 14 July (compared to the rest of the period) for the simulation including (red line) the new parameterization. In this model configuration, the estimated COD reaches values of about ~ 8 for the 10–11 July period, in accordance with the decrease of CER obtained during this period (Figure 18). The second RegCM simulation, which does not include the changes in CER due to aerosols, indicates smaller COD that remains between 3 and 5 for 9 to 14 July. For this period, the parameterization is shown to improve the comparisons of RegCM COD with MODIS observations, even if RegCM COD remains lower.

Smoke particles induce a negative perturbation at TOA between -10 and $-40\ \text{W m}^{-2}$ during the 8 to 14 July period. This significant effect on SW radiative fluxes at TOA estimated by RegCM is absent in MACC reanalysis. This can be due to differences in the aerosol loading, vertical layering in the diagnostic itself, as RegCM simulations do not directly calculate the indirect radiative forcing (contrary to MACC data; see section 3.2) as explained previously. This result indicates that the positive direct forcing exerted by absorbing smoke is probably counterbalanced by a large increase in SW radiations at TOA due to change in the microphysical/optical properties of Sc.

5. Conclusion

The objective of this work is to study the direct and indirect radiative effects of smoke aerosols over California based on the RegCM regional climate model (Giorgi et al., 2012). The representation of biomass-burning radiative properties and aerosol-cloud interactions for smoke particles and marine Sc in the model has been improved. These new radiative properties have been coupled with the RRTM radiative transfer scheme for simulating the SW direct radiative forcing (DRF), in both clear-sky and all-sky conditions. In addition, a new parameterization has been integrated for relating the cloud droplet number concentration (CDNC) and CER to the aerosol number concentration for marine Sc.

The new RegCM configuration has been tested during the extreme biomass-burning period of summer 2008 in California. The RegCM simulations, forced by the APIFLAME biomass-burning emissions inventory, have been performed for the 15 June to 15 July period, and the analyses are focused on 8 to 15 July, when extreme concentration of smoke together with the presence of Sc are observed. The SW smoke optical depth, absorbing properties, heating rate, cloud microphysical/optical (i.e., COD, CDNC and CER) properties, and finally the TOA SW DRF (in clear-sky and all-sky conditions) are particularly investigated.

This study indicates that the intense 2008 fire events are related to significant simulated AOD $\sim 1\text{--}2$ (at $550\ \text{nm}$) near smoke sources. At local scale, RegCM AOD are generally found to be lower than AERONET data, revealing a negative bias between -0.05 and -0.20 (at $550\ \text{nm}$). In parallel, the regional pattern of AOD is well reproduced by RegCM even if the order of magnitude is also found to be lower than OMI or MODIS observations. For cloudy-sky pixels, the comparisons with POLDER ACAOD data demonstrate the ability of RegCM to simulate realistic ACAOD during the transport of smoke above the Pacific Ocean and Sc.

In terms of absorbing properties, the simulated smoke SSA is shown to be around ~ 0.90 (at $550\ \text{nm}$) near biomass-burning sources in accordance with OMI SSA and POLDER ACSSA observations. On the contrary, our results indicate that smoke aerosols appear too absorbing during the transport in the model compared to POLDER data which indicate mostly scattering smoke over the Pacific Ocean. In parallel, simulated AAOD are found to comprise between 0.03 and 0.06 (at $550\ \text{nm}$) near smoke sources and be lower than OMI (~ 0.1) observations. Our analyses indicate also that RegCM is not able to correctly represent the spectral dependence of AAOD leading to AAE of nearly 1 and lower compared to OMI within the smoke plume. Further developments appear necessary (i.e., implementation of brown carbon optical properties) in a future version for improving the spectral dependence of absorbing properties and the potential impact of smoke on UV

radiations. Finally, our results indicate that RegCM simulates diurnal SW heating rates attributable to smoke of $\sim 0.5^\circ\text{K d}^{-1}$ (for ACAOD ~ 0.5).

Concerning the DRF exerted by smoke particles at TOA, an innovative approach has been used here, mainly based on RegCM outputs and POLDER observations. Even if the model is not able (due to its coarse vertical/resolution) to correctly resolve the daily patterns in cloud properties (cloud fraction, liquid water path, and effective radius), one of the main results highlights the ability of RegCM to represent the changes in the sign of the SW TOA DRF exerted by absorbing smoke from clear-sky to all-sky conditions. Indeed, when calculated at 21:00 UTC (corresponding to the time of POLDER overpasses), the RegCM instantaneous DRF is found to be positive ($+2.5 \text{ W m}^{-2}$) in all-sky conditions, in better accordance with POLDER estimates. Such a study underlines the great added value offered by these new remote sensing observations for evaluating radiative forcing estimated by RCM over cloudy scenes.

Finally, the smoke indirect effect is analyzed by implementing a new parameterization, allowing the modification of the Sc CER (and COD) when smoke is transported within clouds. Our results demonstrate that the simulated CER is decreased for the 8 to 14 July period, when the smoke concentration is increasing. During this period, CER is passing from $\sim 10 \mu\text{m}$ to $\sim 6\text{--}7 \mu\text{m}$ at 975 hPa. In accordance with these microphysical changes, the COD increases between 9 and 14 July, reducing the negative bias with MODIS COD observations. These changes in Sc clouds properties lead to a significant perturbation in the net SW radiations at TOA.

Acknowledgments

We acknowledge the AERONET Sun photometer networks and the PIs of the three selected stations and their staff for their work to produce the data set used in this study. MACC was funded by the European Commission under the EU Seventh Research Framework Programme, contract 218793 (data have been downloaded from <http://macc.copernicus-atmosphere.eu/d/services/gac/reanalysis/>). MODIS and OMI data used in this paper were retrieved from the Giovanni online data system (<https://giovanni.gsfc.nasa.gov/giovanni/>), developed and maintained by the NASA GES DISC, as well as ICARE platform. We also acknowledge the Global Modeling and Assimilation Office (GMAO) and the GES DISC for the dissemination of MERRA reanalysis (<https://disc.sci.gsfc.nasa.gov/>). The work performed was also done by using data from EUMETSAT's Satellite Application Facility on Climate Monitoring (CM SAF). The different RegCM simulations, as well as OMI and POLDER Above Clouds AOD, are available on request. We finally thank D. Gazen and the computing support team in Laboratoire d'Aérodynamique.

References

- Abel, S. J., Haywood, J. M., Highwood, E. J., Li, J., and Buseck, P. R. (2003). Evolution of biomass burning aerosol properties from an agricultural fire in southern Africa. *Geophysical Research Letters*, *30*(15), 1783. <https://doi.org/10.1029/2003GL017342>
- Ackerman, S., Toon, O. B., Stevens, D. E., Heymsfield, A. J., Ramanathan, V., & Welton, E. J. (2000). Reduction of tropical cloudiness. *Science*, *288*, 1042–1047.
- Akagi, S. K., Yokelson, R. J., Wiedinmyer, C., Alvarado, M. J., Reid, J. S., Karl, T., ... Wennberg, P. O. (2011). Emission factors for open and domestic biomass burning for use in atmospheric models. *Atmospheric Chemistry and Physics*, *11*, 4039–4072. <https://doi.org/10.5194/acp-11-4039-2011>
- Alexandri, G., Georgoulas, A. K., Zanis, P., Katragkou, E., Tsiokerdekis, A., Kourtidis, K., & Meleti, C. (2015). On the ability of RegCM4 regional climate model to simulate surface solar radiation patterns over Europe: An assessment using satellite-based observations. *Atmospheric Chemistry and Physics*, *15*, 13,195–13,216. <https://doi.org/10.5194/acp-15-13195-2015>
- Allen, G., Coe, H., Clarke, A., Bretherton, C., Wood, R., Abel, S. J., ... Chand, D. (2011). South East Pacific atmospheric composition and variability sampled along 20°S during VOCALS-REx. *Atmospheric Chemistry and Physics*, *11*, 5237–5262. <https://doi.org/10.5194/acp-11-5237-2011>
- Bellouin, N., Rae, J., Jones, A., Johnson, C., Haywood, J., & Boucher, O. (2011). Aerosol forcing in the Climate Model Intercomparison Project (CMIP5) simulations by HadGEM2-ES and the role of ammonium nitrate. *Journal of Geophysical Research: Atmospheres*, *116*, D20206. <https://doi.org/10.1029/2011JD016074>
- Benedetti, A., Morcrette, J.-J., Boucher, O., Dethof, A., Engelen, R. J., Fisher, M., ... Suttie, M. (2009). Aerosol analysis and forecast in the European Centre for Medium-Range Weather Forecasts Integrated Forecast System: 2. Data assimilation. *Journal of Geophysical Research: Atmospheres*, *114*, D13205. <https://doi.org/10.1029/2008JD011115>
- Bougiatioti, A., Stavroulas, I., Kostenidou, E., Zampas, P., Theodosi, C., Kouvarakis, G., ... Mihalopoulos, N. (2014). Processing of biomass-burning aerosol in the eastern Mediterranean during summertime. *Atmospheric Chemistry and Physics*, *14*, 4793–4807. <https://doi.org/10.5194/acp-14-4793-2014>
- Briegleb, B. P. (1992). Delta-Eddington approximation for solar radiation in the NCAR Community Climate Model. *Journal of Geophysical Research: Atmospheres*, *97*, 7603–7612. <https://doi.org/10.1029/92JD00291>
- Brioude, J., Cooper, O. R., Feingold, G., Trainer, M., Freitas, S. R., Kowal, D., ... Hsie, E.-Y. (2009). Effect of biomass burning on marine stratocumulus clouds off the California coast. *Atmospheric Chemistry and Physics*, *9*, 8841–8856. <https://doi.org/10.5194/acp-9-8841-2009>
- Chen, T., Rossow, W. B., & Zhang, Y. C. (2000). Radiative effects of cloud-type variations. *Journal of Climate*, *13*, 264–286.
- Chung, C. E., Kim, S.-W., Lee, M., Yoon, S.-C., & Lee, S. (2012). Carbonaceous aerosol AAE inferred from in-situ aerosol measurements at the Gosan ABC super site, and the implications for brown carbon aerosol. *Atmospheric Chemistry and Physics*, *12*, 6173–6184. <https://doi.org/10.5194/acp-12-6173-2012>
- Clarke, A., McNaughton, C., Kapustin, V., Shinozuka, Y., Howell, S., Dibb, J., ... Pinkerton, M. (2007). Biomass burning and pollution aerosol over North America: Organic components and their influence on spectral optical properties and humidification response. *Journal of Geophysical Research: Atmospheres*, *112*, D12S18. <https://doi.org/10.1029/2006JD007777>
- DeGraaf, M., Bellouin, N., Tilstra, L., Haywood, J., & Stammes, P. (2014). Aerosol direct radiative effect of smoke over clouds over the southeast Atlantic Ocean from 2006 to 2009. *Geophysical Research Letters*, *41*, 7723–7730. <https://doi.org/10.1002/2014GL061103>
- DeGraaf, M., Tilstra, L., Wang, P., & Stammes, P. (2012). Retrieval of the aerosol direct radiative effect over clouds from spaceborne spectroscopy. *Journal of Geophysical Research: Atmospheres*, *117*, D07207. <https://doi.org/10.1029/2011JD017160>
- Dentener, F., Kinne, S., Bond, T., Boucher, O., Cofala, J., Generoso, S., ... Wilson, J. (2006). Emissions of primary aerosol and precursor gases in the years 2000 and 1750 prescribed data-sets for AeroCom. *Atmospheric Chemistry and Physics*, *6*, 4321–4344. <https://doi.org/10.5194/acp-6-4321-2006>
- Dickinson, R. E., Henderson-Sellers, A., & Kennedy, P. J. (1993). Biosphere–Atmosphere Transfer Scheme (BATS) version 1e as coupled to the NCAR Community Climate Model, Tech Rep Nat Center for Atmospheric Research, Boulder, CO.
- Dubovik, O., Holben, B. N., Eck, T. F., Smirnov, A., Kaufman, Y. J., King, M. D., ... Slutsker, I. (2002). Variability of absorption and optical properties of key aerosol types observed in world-wide locations. *Journal of the Atmospheric Sciences*, *59*, 590–608.
- Dubovik, O., & King, M. D. (2000). A flexible inversion algorithm for retrieval of aerosol optical properties from Sun and sky radiance measurements. *Journal of Geophysical Research: Atmospheres*, *105*, 20,673–20,696. <https://doi.org/10.1029/2000JD900282>

- Dubovik, O., Sinyuk, A., Lapyonok, T., Holben, B. N., Mishchenko, M., Yang, P., ... Slutsker, I. (2006). Application of spheroid models to account for aerosol particle nonsphericity in remote sensing of desert dust. *Journal of Geophysical Research: Atmospheres*, *111*, D11208. <https://doi.org/10.1029/2005JD006619>
- Dubovik, O., Smirnov, A., Holben, B. N., King, M. D., Kaufman, Y. J., Eck, T. F., & Slutsker, I. (2000). Accuracy assessments of aerosol properties retrieved from Aerosol Robotic Network (AERONET) Sun and sky measurements. *Journal of Geophysical Research*, *105*, 9791–9806.
- Feng, Y., Ramanathan, V., & Kotamarthi, V. R. (2013). Brown carbon, a significant atmospheric absorber of solar radiations? *Atmospheric Chemistry and Physics*, *13*, 8607–8621.
- Forster, P., Ramaswamy, V., Artaxo, P., Bernsten, T., Betts, R., Fahey, D. W., ... Van Dorland, R. (2007). Changes in atmospheric constituents and in radiative forcing. In S. Solomon, et al. (Eds.), *Climate change 2007: The physical science basis. Contribution of Working Group I to the Fourth Assessment Report of the Intergovernmental Panel on Climate Change* (pp. 131–217). Cambridge, UK and New York: Cambridge University Press.
- Giorgi, F., Coppola, E., Solmon, F., Mariotti, L., Sylla, M. B., Bi, X., ... Brankovic, C. (2012). RegCM4: Model description and preliminary tests over multiple CORDEX domains. *Climate Research*, *52*, 7–29.
- Gyawali, M., Arnott, W. P., Lewis, K., & Moosmüller, H. (2009). In situ aerosol optics in Reno, USA during and after the summer 2008 California wildfires and the influence of absorbing and non-absorbing organic coatings on spectral light absorption. *Atmospheric Chemical and Physics*, *9*, 8007–8015.
- Haywood, J. M., Osborne, S. R., & Abel, S. J. (2004). The effect of overlying absorbing aerosol layers on remote sensing retrievals of cloud effective radius and cloud optical depth. *Quarterly Journal of the Royal Meteorological Society*, *130*, 779–800. <https://doi.org/10.1256/qj.03.100>
- Haywood, J. M., Osborne, S. R., Francis, P. N., Keil, A., Formenti, P., Andreae, M. O., & Kaye, P. H. (2003). The mean physical and optical properties of regional haze dominated by biomass burning aerosol measured from the C-130 aircraft during SAFARI 2000. *Journal of Geophysical Research: Atmospheres*, *108*(D13), 8473. <https://doi.org/10.1029/2002JD002226>
- Hegg, D. A. (1994). Cloud condensation nucleus-sulfate mass relationship and cloud albedo. *Journal of Geophysical Research: Atmospheres*, *99*, 25,903–25,907. <https://doi.org/10.1029/94JD02224>
- Hegg, D. A., Covert, D. S., Jonsson, H. H., & Woods, R. K. (2012). A simple relationship between cloud drop number concentration and precursor aerosol concentration for the regions of Earth's large marine stratocumulus decks. *Atmospheric Chemistry and Physics*, *12*, 1229–1238. <https://doi.org/10.5194/acp-12-1229-2012>
- Hegg, D. A., Nielsen, K., Covert, D. S., Jonsson, H. H., & Durkee, P. A. (2007). Factors influencing the mesoscale variations in marine stratocumulus albedo. *Tellus*, *59B*, 66–76.
- Hildebrandt, L., Engelhart, G. J., Mohr, C., Kostenidou, E., Lanz, V. A., Bougiatioti, A., ... Pandis, S. N. (2010). Aged organic aerosol in the Eastern Mediterranean: The Finokalia Aerosol Measurement Experiment—2008. *Atmospheric Chemistry and Physics*, *10*, 4167–4186. <https://doi.org/10.5194/acp-10-4167-2010>
- IPCC (2013). *Climate change 2013: The physical science basis: Summary for policymakers*. Cambridge, UK: Cambridge University Press.
- Jacobson, M. Z. (2000). A physically based treatment of elemental carbon optics: Implication for global direct forcing of aerosols. *Geophysical Research Letters*, *27*, 217–220. <https://doi.org/10.1029/1999GL010968>
- Jethva, H., Torres, O., & Changwoo, A. (2016). A ten-year global record of absorbing aerosols above clouds from OMI's near-UV observations. *Proc. SPIE 9876, Remote Sensing of the Atmosphere, Clouds, and Precipitation VI*, 9876. 1A. <https://doi.org/10.1117/12.2225765>
- Johnson, B. T., Haywood, J. M., Langridge, J. M., Darbyshire, E., Morgan, W. T., Szpek, K., ... Bellouin, N. (2016). Evaluation of biomass burning aerosols in the HadGEM3 climate model with observations from the SAMBBA field campaign. *Atmospheric Chemistry and Physics*, *16*, 14,657–14,685. <https://doi.org/10.5194/acp-16-14657-2016>
- Johnson, B. T., Shine, K. P., & Forster, P. M. (2004). The semi-direct aerosol effect: Impact of absorbing aerosols on marine stratocumulus. *Quarterly Journal of the Royal Meteorological Society*, *130*, 1407–1422.
- Kalnay, E., Kanamitsu, M., Kistler, R., Collins, W., Deaven, D., Gandin, L., ... Joseph, D. (1996). The NCEP/NCAR 40-year reanalysis project. *Bulletin of the American Meteorological Society*, *77*, 437–470.
- King, M. D., Radke, L. F., & Hobbs, P. V. (1993). Optical properties of marine stratocumulus clouds modified by ships. *Journal of Geophysical Research: Atmospheres*, *98*(D2), 2729–2739. <https://doi.org/10.1029/92JD02082>
- Klein, S. A., & Hartmann, D. L. (1993). The seasonal cycle of low stratiform clouds. *Journal of Climate*, *6*, 1588–1606.
- Krinner, G., Viovy, N., de Noblet-Ducoudre, N., Ogee, J., Polcher, J., Friedlingstein, P., ... Prentice, I. (2005). A dynamic global vegetation model for studies of the coupled atmosphere-biosphere system. *Global Biogeochemical Cycles*, *19*, GB1015. <https://doi.org/10.1029/2003GB002199>
- Labonne, M., Breon, F.-M., & Chevallier, F. (2007). Injection height of biomass burning aerosols as seen from a spaceborne lidar. *Geophysical Research Letters*, *34*, L11806. <https://doi.org/10.10292007GL029311>
- Levelt, P. F., Hilsenrath, E., Leppelmeier, G. W., van den Oord, G. H. J., Bhartia, P. K., Tamminen, J., ... Veefkind, J. P. (2006). Science objectives of the Ozone Monitoring Instrument. *IEEE Transactions on Geoscience and Remote Sensing*, *44*, 1199–1208.
- Li, S., Wang, T., Solmon, F., Zhuang, B., Wu, H., Xie, M., ... Wang, X. (2016). Impact of aerosols on regional climate in southern and northern China during strong/weak East Asian summer monsoon years. *Journal of Geophysical Research: Atmospheres*, *121*, 4069–4081. <https://doi.org/10.1002/2015JD023892>
- Malavelle, F., Pont, V., Mallet, M., Solmon, F., Johnson, B., Leon, J.-F., & Liousse, C. (2011). Simulation of aerosol radiative effects over West Africa during DABEX and AMMA SOP-0. *Journal of Geophysical Research: Atmospheres*, *116*, D08205. <https://doi.org/10.1029/2010JD014829>
- Martin, G. M., Johnson, D. W., & Spice, A. (1994). The measurement and parameterization of effective radius of droplets in warm stratocumulus clouds. *Journal of the Atmospheric Sciences*, *51*, 1823–1842.
- McComiskey, A., Feingold, G., Frisch, A., Turner, D., Miller, M., Chiu, J., ... Ogren, J. (2009). An assessment of aerosol-cloud interactions in marine stratus clouds based on surface remote sensing. *Journal of Geophysical Research: Atmospheres*, *114*, D09203. <https://doi.org/10.1029/2008JD011006>
- Menon, S., Del Genio, A. D., Kaufman, Y., Bennartz, R., Koch, D., Loeb, N., & Orlikowski, D. (2008). Analyzing signatures of aerosol-cloud interactions from satellite retrievals and the GISS GCM to constrain the aerosol indirect effect. *Journal of Geophysical Research: Atmospheres*, *113*, D14S22. <https://doi.org/10.1029/2007JD009442>
- Meyer, K., Platnick, S., & Zhang, Z. (2015). Simultaneously inferring above-cloud absorbing aerosol optical thickness and underlying liquid phase cloud optical and microphysical properties using MODIS. *Journal of Geophysical Research: Atmospheres*, *120*, 5524–5547. <https://doi.org/10.1002/2015JD023128>

- Mlawer, E. J., Taubman, S. J., Brown, P. D., Iacono, M. J., & Clough, S. A. (1997). Radiative transfer for inhomogeneous atmospheres: RRTM, a validated correlated- k model for the longwave. *Journal of Geophysical Research: Atmospheres*, *102D*, 16,663–16,682. <https://doi.org/10.1029/97JD00237>
- Morcrette, J.-J., Boucher, O., Jones, L., Salmond, D., Bechtold, P., Beljaars, A., ... Untch, A. (2009). Aerosol analysis and forecast in the European Centre for Medium-Range Weather Forecasts integrated forecast system: Forward modelling. *Journal of Geophysical Research: Atmospheres*, *114*, D06206. <https://doi.org/10.1029/2008JD011235>
- Myhre, G., Samset, B. H., Schulz, M., Balkanski, Y., Bauer, S., Bernsten, T. K., ... Zhou, C. (2013). Radiative forcing of the direct aerosol effect from AeroCom Phase II simulations. *Atmospheric Chemistry and Physics*, *13*(4), 1853–1877. <https://doi.org/10.5194/acp-13-1853-2013>
- Nakajima, T. Y., Suzuki, K., & Stephens, G. L. (2010). Droplet growth in warm water clouds observed by the A-Train. Part I: Sensitivity analysis of the MODIS-derived cloud droplet sizes. *Journal of the Atmospheric Sciences*, *67*, 1884–1894. <https://doi.org/10.1175/2009JAS3280.1>
- Naud, C. M., Booth, J. F., & Del Genio, A. D. (2014). Evaluation of ERA-Interim and MERRA cloudiness in the Southern Ocean. *Journal of Climate*, *27*(2), 109–124. <https://doi.org/10.1175/2009JAS3280.1>
- Noble, S. R., & Hudson, J. G. (2015). MODIS comparisons with northeastern Pacific in situ stratocumulus microphysics. *Journal of Geophysical Research: Atmospheres*, *120*, 8332–8344. <https://doi.org/10.1002/2014JD022785>
- O'Brien, T. A., Chuang, P. Y., Sloan, L. C., Faloona, I. C., & Rossiter, D. L. (2012). Coupling a new turbulence parametrization to RegCM adds realistic stratocumulus clouds. *Geoscientific Model Development*, *5*, 989–1008. <https://doi.org/10.5194/gmd-5-989-2012>
- Oreopoulos, L., & Khairoutdinov, M. (2003). Overlap properties of clouds generated by a cloud-resolving model. *Journal of Geophysical Research: Atmospheres*, *108*(D15), 4479. <https://doi.org/10.1029/2002JD003329>
- Painemal, D., & Minnis, P. (2012). On the dependence of albedo on cloud microphysics over marine stratocumulus clouds regimes determined from Clouds and the Earth's Radiant Energy System (CERES) data. *Journal of Geophysical Research: Atmospheres*, *117*, D06203. <https://doi.org/10.1029/2011JD017120>
- Painemal, D., & Zuidema, P. (2011). Assessment of MODIS cloud effective radius and optical thickness retrievals over the Southeast Pacific with VOCALS-Rex in-situ measurements. *Journal of Geophysical Research: Atmospheres*, *116*, D24206. <https://doi.org/10.1029/2011JD016155>
- Peers, F., Waquet, F., Cornet, C., Dubuisson, P., Ducos, F., Goloub, P., ... Thieuleux, F. (2015). Absorption of aerosols above clouds from POLDER/PARASOL measurements and estimation of their direct radiative effect. *Atmospheric Chemistry and Physics*, *15*(8), 4179–4196.
- Pfister, G. G., Wiedinmyer, C., & Emmons, L. K. (2008). Impacts of the fall 2007 California wildfires on surface ozone: Integrating local observations with global model simulations. *Geophysical Research Letters*, *35*, L19814. <https://doi.org/10.1029/2008GL034747>
- Pringle, K. J., Carslaw, K. S., Spracklen, D. V., Mann, G. M., & Chipperfield, M. P. (2009). The relationship between aerosol and cloud drop number concentrations in a global aerosol microphysics model. *Atmospheric Chemistry and Physics*, *9*, 4131–4144. <https://doi.org/10.5194/acp-9-4131-2009>
- Qian, Y., & Giorgi, F. (1999). Interactive coupling of regional climate and sulfate aerosol model over eastern Asia. *Journal of Geophysical Research: Atmospheres*, *104*, 6477–6500. <https://doi.org/10.1029/98JD02347>
- Quaas, J., Boucher, O., Bellouin, N., & Kinne, S. (2008). Satellite-based estimate of the direct and indirect aerosol climate forcing. *Journal of Geophysical Research: Atmospheres*, *113*, D05204. <https://doi.org/10.1029/2007JD008962>
- Randall, D. A., Coakley, J. A., Fairall, C. W., Knopfl, R. A., & Lenschow, D. H. (1984). Outlook for research on marine subtropical stratocumulus clouds. *Bulletin of the American Meteorological Society*, *65*, 1290–1301.
- Reid, J. S., & Hobbs, P. V. (1998). Physical and optical properties of young smoke from individual biomass fires in Brazil. *Journal of Geophysical Research: Atmospheres*, *103*, 32,013–32,031. <https://doi.org/10.1029/98JD00159>
- Remer, L. A., Kaufman, Y. J., Tanré, D., Mattoo, S., Chu, D. A., Martins, J. V., ... Holben, B. N. (2005). The MODIS aerosol algorithm, products, and validation. *Journal of the Atmospheric Sciences*, *62*, 947–973. <https://doi.org/10.1175/JAS3385.1>
- Reynolds, R. W., Rayner, N. A., Smith, T. M., Stokes, D. C., & Wang, W. (2002). An improved in situ and satellite SST analysis for climate. *Journal of Climate*, *15*, 1609–1625.
- Rienecker, M. M., Suarez, M. J., Gelaro, R., Todling, R., Bacmeister, J., Liu, E., ... Woollen, J. (2011). MERRA: NASA's Modern-Era Retrospective Analysis for Research and Applications. *Journal of Climate*, *24*, 3624–3648.
- Rissler, J., Vestin, A., Swietlicki, E., Fisch, G., Zhou, J., Artaxo, P., & Andreae, M. O. (2006). Size distribution and hygroscopic properties of aerosol particles from dry-season biomass burning in Amazonia. *Atmospheric Chemistry and Physics*, *6*, 471–491. <https://doi.org/10.5194/acp-6-471-2006>
- Rodwell, M. J., & Jung, T. (2008). Understanding the local and global impacts of model physics changes: An aerosol example. *Quarterly Journal of the Royal Meteorological Society*, *134*, 1479–1497. <https://doi.org/10.1002/qj.298>
- Russell, P. B., Bergstrom, R. W., Shinozuka, Y., Clarke, A. D., De-Carlo, P. F., Jimenez, J. L., ... Strawa, A. (2010). Absorption Angstrom Exponent in AERONET and related data as an indicator of aerosol composition. *Atmospheric Chemistry and Physics*, *10*, 1155–1169. <https://doi.org/10.5194/acp-10-1155-2010>
- Sciare, J., Oikonomou, K., Cachier, H., Mihalopoulos, N., Andreae, M. O., Maenhaut, W., & Sarda-Estève, R. (2005). Aerosol mass closure and reconstruction of the light scattering coefficient over the Eastern Mediterranean Sea during the MINOS campaign. *Atmospheric Chemistry and Physics*, *5*, 2253–2265. <https://doi.org/10.5194/acp-5-2253-2005>
- Shindell, D. T., Lamarque, J. F., Schulz, M., Flanner, M., Jiao, C., Chin, M., ... Lo, F. (2013). Radiative forcing in the ACCMIP historical and future climate simulations. *Atmospheric Chemistry and Physics*, *13*, 2939–2974. <https://doi.org/10.5194/acp-13-2939-2013>
- Solmon, F., Elguindi, N., & Mallet, M. (2012). Evaluation of dust aerosol climatic impacts over West Africa as simulated by a regional climate model. *Climate Research*, *52*, 97–113.
- Solmon, F., Giorgi, F., & Lioussé, C. (2006). Aerosol modelling for regional climate studies: Application to anthropogenic particles and evaluation over a European/African domain. *Tellus Series B*, *58*(1), 51–72. <https://doi.org/10.1111/j.1600-0889.2005.00155.x>
- Solmon, F., Mallet, M., Elguindi, N., Giorgi, F., Zakey, A., & Konaré, A. (2008). Dust aerosol impact on regional precipitation over western Africa, mechanisms and sensitivity to absorption properties. *Geophysical Research Letters*, *35*, L24705. <https://doi.org/10.1029/2008GL035900>
- Solmon, F., Nair, V. S., & Mallet, M. (2015). Increasing Arabian dust activity and the Indian summer monsoon. *Atmospheric Chemistry and Physics*, *15*, 8051–8064. <https://doi.org/10.5194/acp-15-8051-2015>
- Stier, P., Schutgens, N. A. J., Bellouin, N., Bian, H., Boucher, O., Chin, M., ... Zhou, C. (2013). Host model uncertainties in aerosol radiative forcing estimates: Results from the AeroCom prescribed intercomparison study. *Atmospheric Chemistry and Physics*, *13*(6), 3245–3270. <https://doi.org/10.5194/acp-13-3245-2013>
- Torres, O., Jethva, H., & Bhartia, P. K. (2012). Retrieval of aerosol optical depth above clouds from OMI observations: Sensitivity analysis and case studies. *Journal of the Atmospheric Sciences*, *69*, 1037–1053. <https://doi.org/10.1175/JAS-D-11-0130.1>

- Torres, O., Tanskanen, A., Veihelman, B., Ahn, C., Braak, R., Bhartia, P. K., ... Levelt, P. (2007). Aerosols and surface UV products from OMI observations: An overview. *Journal of Geophysical Research: Atmospheres*, *112*, D24S47. <https://doi.org/10.1029/2007JD008809>
- Tsikerdekis, A., Zanis, P., Steiner, A. L., Solmon, F., Amiridis, V., Marinou, E., ... Foret, G. (2017). Impact of dust size parameterizations on aerosol burden and radiative forcing in RegCM4. *Atmospheric Chemistry and Physics*, *17*, 769–791. <https://doi.org/10.5194/acp-17-769-2017>
- Tummon, F., Solmon, F., Liousse, C., & Tadross, M. (2010). Simulation of the direct and semidirect aerosol effects on the southern Africa regional climate during the biomass burning season. *Journal of Geophysical Research: Atmospheres*, *115*, D19206. <https://doi.org/10.1029/2009JD013738>
- Turquet, S., Menut, L., Bessagnet, B., Anav, A., Viovy, N., Maignan, F., & Wooster, M. (2014). APIFLAME v1.0: High-resolution fire emission model and application to the Euro-Mediterranean region. *Geoscientific Model Development*, *7*, 587–612. <https://doi.org/10.5194/gmd-7-587-2014>
- Twohy, C. H., Petters, M. D., Snider, J. R., Stevens, B., Tahnk, W., Wetzell, M., ... Burnet, F. (2005). Evaluation of the aerosol indirect effect in marine stratocumulus clouds: Droplet number, size, liquid water path, and radiative impact. *Journal of Geophysical Research: Atmospheres*, *110*, D08203. <https://doi.org/10.1029/2004JD005116>
- Waquet, F., Cornet, C., Deuzé, J. L., Dubovik, O., Ducos, F., Goloub, P., ... Tanré, D. (2013). Retrieval of aerosol microphysical and optical properties above liquid clouds from POLDER/PARASOL polarization measurements. *Atmospheric Measurement Techniques*, *6*(4), 991–1016.
- Waquet, F., Peers, F., Ducos, F., Goloub, P., Platnick, S., Riedi, J., ... Thieuleux, F. (2013). Global analysis of aerosol properties above clouds. *Geophysical Research Letters*, *40*, 5809–5814. <https://doi.org/10.1002/2013GL057482>
- Westerling, A. L., Hidalgo, H. G., Cayan, D. R., & Swetnam, T. W. (2006). Warming and earlier spring increase Western U.S. Forest Wildfire Activity. *Science*, *313*, 940–943.
- Wilcox, E. M. (2010). Stratocumulus cloud thickening beneath layers of absorbing smoke aerosol. *Atmospheric Chemistry and Physics*, *10*, 11,769–11,777. <https://doi.org/10.5194/acp-10-11769-2010>
- Wood, R. (2012). Review stratocumulus clouds. *Monthly Weather Review*, *140*, 2373–2423.
- Xu, H., Guo, J. P., Ceamanos, X., Roujean, J. L., Min, M., & Carrer, D. (2016). On the influence of the diurnal variations of aerosol content to estimate direct aerosol radiative forcing using MODIS data. *Atmospheric Environment*, *141*, 186–196. <https://doi.org/10.1016/j.atmosenv.2016.06.067>
- Yin, C., Wang, T., Solmon, F., Mallet, M., Jiang, F., Li, S., & Zhuang, B. (2015). Assessment of direct radiative forcing due to secondary organic aerosol with regional climate model. *Tellus B*, *67*, 24634.
- Zakey, A. S., Solmon, F., & Giorgi, F. (2006a). Implementation and testing of a desert dust module in a regional climate model. *Atmospheric Chemistry and Physics*, *6*(12), 4687–4704. <https://doi.org/10.5194/acp-6-4687-2006>
- Zakey, A. S., Solmon, F., & Giorgi, F. (2006b). Development and testing of a desert dust module in a regional climate model. *Atmospheric Chemistry and Physics*, *6*, 1749–1792.
- Zanis, P., Ntografas, C., Zakey, A., Pytharoulis, I., & Karacostas, T. (2012). Regional climate feedback of anthropogenic aerosols over Europe using RegCM3. *Climate Research*, *52*, 267–278. <https://doi.org/10.3354/cr01070>
- Zhang, Z., & Platnick, S. (2011). An assessment of differences between cloud effective particle radius retrievals for marine water clouds from three MODIS spectral bands. *Journal of Geophysical Research: Atmospheres*, *116*, D20215. <https://doi.org/10.1029/2011JD016216>
- Zhuang, B. L., Wang, T. J., Liu, J., Li, S., Xie, M., Han, Y., ... Zhu, J. L. (2017). The surface aerosol optical properties in urban areas of Nanjing, west Yangtze River Delta, China. *Atmospheric Chemistry and Physics*, *17*, 1143–1160. <https://doi.org/10.5194/acp-17-1143-2017>